This is a preprint, the final version is subject to change, of the American Mineralogist (MSA)
Cite as Authors (Year) Title. American Mineralogist, in press.
DOI: https://doi.org/10.2138/am-2018-6316

REVISION 2

Micro- and nano-scale study of deformation induced mineral transformations in Mg-phyllosilicate-rich fault gouges from the Galera Fault Zone (Betic Cordillera, SE Spain)

CATALINA SÁNCHEZ-ROA (1) *, BLANCA BAULUZ (2), FERNANDO NIETO (3), ISABEL ABAD (1), JUAN JIMENÉZ-MILLÁN (1) DANIEL FAULKNER (4).

(1) Departamento de Geología and CEACTierra, Unidad Asociada IACT (CSIC-UGR), Universidad de Jaén, Campus Las Lagunillas s/n, 23071 Jaén, Spain, (2), IUCA-Facultad de Ciencias, Universidad de Zaragoza, Pedro Cerbuna 12, Zaragoza, Spain, (3) Departamento de Mineralogía y Petrología and IACT (CSIC-UGR), Facultad de Ciencias, Universidad de Granada, Avda. Fuentenueva s/n, 18002 Granada, Spain, (4) Rock Deformation Laboratory, Department of Earth, Ocean and Ecological Sciences, University of Liverpool, Liverpool, UK.

Abstract

Naturally and experimentally deformed gouges from sliding surfaces within the Galera Fault Zone were analyzed using scanning and transmission electron microscopy (SEM, TEM) to identify changes in the fault rocks as a consequence of ongoing deformation. The two gouges studied have a particular mineral association that includes planar (mainly smectite and illite) and fibrous clay minerals (sepiolite and palygorskite). Microstructural findings include a radical difference in grain alignment between the two gouges, a phenomenon that strongly influences gouge permeability. Smectite crystals are aligned on the same orientation and show a great number of layer terminations and delamination on the basal planes that contribute to a distributed mode of deformation in the gouge. In contrast, the sepiolite-rich gouge exhibits a grid-like microfabric that results in localized deformation limited to small areas where the needle-like crystals are bent and broken producing "feather-like" structures, without the presence of

lattice distortions. Meanwhile, significant chemical results include: 1. Al content identified in sepiolite fibers through Analytical Electron Microscopy (AEM), together with variability in the (110) d-spacing of sepiolite across single fibers, suggest the existence of a progressive transformation from sepiolite to palygorskite; 2. Mg content in smectite suggests that a portion of the smectites within the fault plane could have an authigenic origin and may be the result of a transformation reaction from palygorskite, however the similarity of the 2:1 layer compositions between the smectites in the two contexts do not allow to either confirm nor deny such possibility. 3. Chemical continuity of Mg-decrease and Al+Fe-increase in the octahedral cation content of the sepiolites, palygorskites and smectites within the gouges indicate a sequence of mineral transformations that is favored by a depleted Mg content and an increase of Al content in the fluid. In this setting, deformation promotes grain size reduction and fluid-rock interaction with the wall rocks resulting in a local supply of Al to the fault gouge that drives phase transformations. Structural differences between smectites and fibrous clay minerals affect important chemical and physical properties of the gouge including their mechanical properties. We propose that the permeability of the gouges in the Galera Fault is strongly affected by their mineralogy. Furthermore, the extent of the mineral authigenesis and mineral transformations could be a controlling factor that progressively change both the permeability and the strength of the fault.

Keywords:

Fibrous clay minerals, mineral transformations, fault zones, mineralogy of fault rocks, sepiolite, palygorskite, smectite, HR-TEM.

49

50

This is a preprint, the final version is subject to change, of the American Mineralogist (MSA)
Cite as Authors (Year) Title. American Mineralogist, in press.
DOI: https://doi.org/10.2138/am-2018-6316

REVISION 2

1. Introduction

Active faulting is an important phenomenon triggering chemical and physical processes in the rocks involved (Hickman et al., 1995; Faulkner et al., 2010). Chemical processes involve element mobility and redistribution assisted by fluids flowing through the faults. These fluids can either come from deep sources as in the case of hot springs, basin brines, hydrothermal and metamorphic fluids, or meteoric waters infiltrating through the newly-formed cracks in the rock. Significant evidence of the chemical reactions that occur in this setting include changes in the mineralogy of the fault gouge and adjacent rock (e.g., Sibson et al., 1979; Cox et al., 2001; Schleicher et al., 2006; 2012). Physical processes on the other hand are related to how minerals accommodate deformation under high levels of strain, commonly experienced on fault planes. A previous study of the mineralogy of the Galera Fault (SE Spain) documented the presence of authigenic Mg-rich fibrous clay minerals within the fault planes as a consequence of the fluid-rock interactions favored by active faulting (Sánchez-Roa et al., 2016). The two types of fault gouge in the Galera Fault present different resistance to shear due to the authigenic minerals concentrated in each section of the fault: the gouge to the south-west, which is rich in fibrous clay minerals has a higher friction coefficient (μ=0.47 under wet deformation); meanwhile the gouge recovered close to the town of Galera is rich in smectite with a small amount of fibrous minerals and has a lower friction coefficient (μ=0.17 under wet deformation) (Sánchez-Roa et al., 2016). The contrasting mechanical behavior between the two gouges motivates the study of the textural evolution and mineral transformations that can contribute to a differential resistance to shear during active faulting.

Permeability is an important parameter in fault zones and is impacted by fundamental parameters such as the host rock lithology, fault activity, magnitude of displacement, pre-existing structures, the depth, the tectonic stress field and the width of the deformed zone (Houwers et al., 2015). The rock texture and its influence in the permeability of the two gouge types of the

Galera Fault Zone can be explored through scanning and transmission electron microscopy (SEM and TEM). A micro- and nano-scale study of these fault rocks could provide a deeper insight into the deformation mechanisms in phyllosilicates. Planar phyllosilicates commonly deform through delamination, fracturing, kinking and dislocation glide (Ibanez and Kronenberg, 1993; Mares and Kronenberg, 1993; Sánchez-Navas and Galindo-Zaldívar, 1993; French et al., 2015). Delamination often occurs during frictional sliding in phyllosilicates with low interlayer electrostatic separation energy (Moore and Lockner, 2004), as is the case for talc and pyrophyllite (Giese, 1978; Sakuma and Suehara, 2015). However, little is known about the possible deformation mechanisms and fluid/mineral interactions occurring in fibrous materials such as the fibrous clay minerals or a mixed regime where both fibrous and planar phyllosilicates are present.

TEM study of clay minerals is challenging due to their susceptibility to electron beam damage, which is mainly related to the diffusion of alkali elements induced by the high voltages of the electron beam (van der Pluijm et al., 1988; Peacor, 1992). These observations remain true for the fibrous clay mineral group (sepiolite and palygorskite), where the cause of instability under the electron beam has been previously attributed to the high percentage of H_2O and mobile cations within the zeolite-like channels (Krekeler and Guggenheim, 2008). Most work on the microscopic properties of these minerals has been achieved by separating individual particles, however the investigation of their mineral transformations and their contribution to the fabric of rocks is still to be explored. Thus, the study of these minerals and their texture in the context of active deformation is poorly understood and requires TEM exploration.

In this study, we investigate naturally and experimentally deformed fault gouge samples from two main shear zones within the Galera Fault Zone by SEM and TEM. The aim of the study is to identify the microstructural features and mineral transformations that contribute to

differences in the resistance to shear between the two main shear zones of the Galera Fault Zone.

2. Geological setting and materials

The Galera Fault Zone is an active strike-slip fault (Fig. 1), located in the Betic Cordillera of southeast Spain within the Guadix-Baza Basin (García-Tortosa et al., 2011). The Galera Fault has an extension of approximately 23 km long and 1.5 km wide with orientation N50°E. The structure is associated with a NE–SW elongated asymmetric anticline and consists of several parallel splays dipping 40° to 60° NW (Sánchez-Roa et al., 2016). The sedimentary sequence of the wall rock presents an alternation of white marls and dark lutitic layers that contain dolomite, gypsum, quartz, calcite and phyllosilicates in their mineral assemblages. Two distinct minerals assemblages have been identified within the fault planes and are focus of this study. The first consists of smectite- and palygorskite-rich fault gouges at the central area of the fault (Galera Village); the second consists of a sepiolite-rich gouge mainly at the SW segment of the fault (Rambla de los Pilares). Fibrous clay-rich gouges are enriched in Mg due to hydrothermal alteration during periods of fluid-rock interaction, concentrated in fault planes and fractures (Sánchez-Roa et al., 2016).

3. Methods

3.1. Sample preparation

The preparation of samples for High-Resolution (HR-) TEM observation had three different procedures:

3.1.1 Impregnation with London Resin White (LRW) and ion thinning

Samples selected for microstructural analysis were prepared using a method modified from Kim et al. (1995). The method involves a multi-step exchange of the sample material with ethanol (99.9%) and London Resin White under refrigeration. The aim of the impregnation is to preserve the texture and the permanent expansion of smectite interlayers for TEM observation.

The impregnation of samples involves a hydration phase, where air-dried rock pieces were placed on a grid suspended over water creating a water steam saturated atmosphere. The samples were left for rehydration over a period of 48 hours. During the embedding phase: The water in the clay is replaced by ultra-pure ethanol of 99.9% purity. The samples were immersed in 100% ethanol for two periods of two hours and one of four hours. The LRW is progressively added in different mixtures of ethanol and LRW with volume ratios of ½, ⅓ and ¼ each for two hours and then immersed in pure LRW overnight in a refrigerator. The next day the LRW was changed twice after periods of four hours. Finally, in the polymerization phase, fresh LRW was added to the samples and placed in an oven at 60 °C for 24h to polymerize and harden the LRW. The vacuum desiccator step (Kim et al., 1995), was not fully carried out due to the fragile nature of the samples.

The cured samples were cut perpendicular to the shear plane, in the direction of shear and an ordinary thin section was then prepared using a diamond saw with oil as lubricant to shape the samples. Sticky wax was used as an adhesive to bond the sample and the thin section glass.

This is a preprint, the final version is subject to change, of the American Mineralogist (MSA)
Cite as Authors (Year) Title. American Mineralogist, in press.
DOI: https://doi.org/10.2138/am-2018-6316

Several 3 mm copper rings with a 1 mm hole in diameter were glued with an epoxy resin to the areas selected for further study. After drying for 24 hours, the rings were removed by heating the thin section. The rings were cleaned and ion-thinned to a suitable thickness for TEM study in a Fischione-1010 ion mill (Universidad de Jaén). The initial conditions for the ion thinning were 12°, 5kV and 5mA until the first hole opened, from there they had an intermediate stage with 8°, 4kV and 5mA, followed by a final stage with 5°, 3kV and 5mA.

3.1.2 Impregnation with Epothin resin and FIB-SEM

Sample preparation through the second method included an impregnation of the samples in EpoThin resin and hardener in a ratio of 2:1 and hardened under vacuum. The blocks were polished using silicon carbide powder and both isopropanol and mineral oil as lubricant agent. The polished blocks were observed under a Dual Beam Ariga Zeiss FIB-SEM (Focused Ion Beam-Scanning Electron Microscope) mainly operated at 30kV (Universidad de Sevilla). The objective of using the technique is to identify the most interesting areas for observation while keeping the fabric and structural context of the extracted lamellae. The FIB-SEM technique combines imaging capabilities of the electron beam and milling capabilities of the ion beam allowing the selection of suitable sampling sites with signs of higher deformation and micro-scale sectioning of electron transparent foils for TEM analysis. The selected area is marked and trenched using a focused beam of Ga^+ ions (Overwijk, 1993), the initial intensity for trenching was set to 20 nA for one hour and then set to 4 nA until the end of the trenching process. The procedure leaves a narrow slice standing and pending by one of the uncut edges. The slice was then welded by depositing a Pt-binding agent and was fixed to a half-copper-washer for TEM observation.

3.1.3 Particle dispersion

Powders of the natural samples were prepared using holey carbon-coated Cu grids. The powder was dispersed in ultra-pure ethanol and immersed in the ultrasonic bath for 15 seconds. This

preparation disperses individual grains of minerals onto the grid surface. The analyses performed on individual crystals allow a larger area to be used in the scanning transmission electron microscopy (STEM) mode for the chemical quantitative analysis and provides better reproducibility of data due to the decrease in alkali loss. Although the powdered samples offer better analytical quality, the ion-milled samples offer textural information of the analyzed grains (Abad et al., 2002).

In addition to the natural samples, homoionized specimens of the smectite-rich sample were also analyzed using this particle dispersion method to reveal the possible presence of interlayer Mg.

3.2. Analytical techniques

Scanning Electron Microscopy (SEM)

Textural observations were made on polished impregnated blocks in secondary electron mode (SE) and backscattered electron mode (BSE). The SEM study was carried out with a Merlin Carl Zeiss field emission (FE) SEM in the Centro de Instrumentación Científico-Técnica of the Universidad de Jaén.

High-Resolution Transmission Electron Microscopy (HR-TEM)

The TEM images were obtained using three instruments: a JEOL-2000-FX-II TEM at the University of Zaragoza operated at 200 kV; a FEI TITAN G2 TEM in the Centro de Instrumentación Científica (C.I.C.) of the Universidad de Granada, operated at 300 kV, with XFEG emission gun, spherical aberration corrector and HAADF detector, with a resolution of 0.8 Å in the TEM mode and 2 Å in the scanning TEM mode; and a FEI TITAN High-Base TEM in the Laboratorio de Microscopias Avanzadas at the Universidad de Zaragoza, operated at 300 kV, with Schottky-FEG emission gun, spherical aberration corrector (CETCOR, CEOS company), HAADF detector, and a 2k x 2k CCD Gatan camera, with a resolution of 0.9 Å in the

192 TEM mode.

193 Analytical Electron Microscopy (AEM)

194 Chemical analyses (TEM-AEM) were obtained with two instruments: a Philips CM20 (C.I.C.,
195 Universidad de Granada), operating at 200 kV in STEM mode, with an EDAX solid-state energy
196 dispersive X-ray (EDX) detector and with a scan window of ~20 Å~ 100 nm for the analysis of
197 individual clay particles; the second instrument is a FEI TITAN Low-base TEM in the
198 Laboratorio de Microscopias Avanzadas at the Universidad de Zaragoza, operated at 300 kV,
199 with a high brightness field emission gun (XFEG), a monochromator unit, a spherical aberration
200 corrector (CETCOR, CEOS company), HAADF detector, and a 2k x 2k CCD Gatan camera,
201 with a resolution of 0.9 Å. The analyses were obtained in the HRSTEM mode. The following
202 minerals were used to obtain the k factors for the transformation of intensity radiuses towards
203 concentration ratios in accordance with the approximation made by Cliff and Lorimer (1975):
204 albite, olivine, biotite, spessartine, muscovite, chlorite and titanite.

205 Structural formulas of smectites were calculated from AEM data after analyzing 103 crystals. The
206 results were normalized to $O_{10}(OH)_2$ and all Fe was considered as Fe^{3+}. The normalization
207 procedure shows a sum of octahedral cations higher than 2.1 per formula unit (a.f.u.) for 43% of
208 the analyzed crystals indicating a divergence from their dioctahedral character. In addition, the
209 sum of interlayer cations is lower than 0.2 a.f.u. for 32.5% and lower than 0.3 for 53.9% of the
210 analyzed crystals. These results suggest the possibility that some of the Mg^{2+} that was originally
211 considered octahedral is instead located in the interlayer. Analyses on smectite particles from the
212 samples homoionized with K and Ca show: a strong decrease in Mg content, an octahedral
213 population very close to 2 a.f.u., and normal values of interlayer population. Based on these
214 results, the total Mg^{2+} of the natural samples was redistributed within interlayer and octahedral
215 positions to ensure that the octahedral sheet keeps a dioctahedral character and that the
216 interlayer charge remains within the normal range for smectites (0.2 to 0.6).

3.3. Permeability measurements

Permeability tests were carried out on a triaxial deformation apparatus with a servo-controlled axial loading system and fluid pressure pump (Mitchell and Faulkner, 2008) in the Rock Deformation Laboratory in the University of Liverpool. The apparatus is capable of applying confining pressures of up to 250 MPa and pore pressures up to 200 MPa. It measures ultra-low permeability down to 10^{-22} m^2 and a sample volume change of 0.1 mm^3. The servo-controlled pore fluid system controls pore fluid pressure and serves as a high precision volumometer. This system can be used to measure permeability through various methods including the pulse transient technique (Brace et al., 1968) applied in this study to obtain values of permeability for the fault gouges at different confining pressures. The gouge powders were prepared by mixing 0.4 g of the sample with 0.5 mL of distilled water. The paste was then placed between two sintered discs with a known permeability of 10^{-13} m^2. The discs holding a cylindrical gouge layer approximately 1 mm high were placed within a PVC jacket and coupled with the sample assembly. Once the sample was inside the pressure vessel, the confining and pore pressure were progressively increased from a pore pressure value of 5 MPa that was kept for all measurements and an initial confining pressure of 10 MPa. The confining pressure was progressively increased in 20 MPa intervals to obtain permeability measurements at 5, 20, 40, 60, 80, and 100 MPa effective pressure. The pressure was left to equilibrate after each pressure increase until no changes in either pore or confining pressure were observed. The samples were recovered after depressurization and carefully measured to determine the final sample thickness and calculate permeability values. The pulse transient technique imposes a 1 MPa pressure differential in the upstream reservoir and bases the calculations on how this pressure increase is transmitted through the gouge sample to determine permeability (Brace et al., 1968).

4. Results

4.1 SEM observations

4.1.1 Naturally deformed fault rocks

a. Smectite- and palygorskite-rich fault gouge

BSE-SEM observations of the fault gouge from the Galera town area show that the rock is composed of a very fine grain phyllosilicate-rich matrix that constitutes the majority of the rock and surrounds micron-size clasts of dolomite, orthoclase and quartz. Deformation features in the sample include the presence of bands of very fine grain minerals alternated with bands of coarser minerals that suggest cataclastic processes including grain rotation and grain size reduction (Fig. 2). The observed structural features of the sample include the alignment of platy clay minerals in an orientation similar to the shear direction, between 135° and 180° to the shear vector (Rutter et al., 1986), hereafter called the P-foliation after Logan et al. (1979). A set of shears that transect the P-foliation were also identified in the gouge and correspond with the definition of R_1 (Riedel) shears according to Logan et al., (1979). The gouge also exhibits surfaces parallel to the shear zone and with the same sense of shear, here referred to as Y surfaces (Logan et al., 1979).

b. Sepiolite-rich fault gouge

Low magnification BSE images of the sepiolite-rich fault gouge show a homogeneous gouge with very fine grain size sepiolite that constitutes the majority of the sample (Fig. 3a). Deformation features are observed in the larger grain size phases that show mica-delamination and broken and aligned grains (Fig. 3a), however due to the clay size of the matrix further examination is restricted. Secondary electron image using in-lens detector of the gouge matrix shows fibrous sepiolite crystals with mainly two preferred orientations perpendicular to each other forming the majority of the gouge matrix (Fig. 3b).

264 **4.1.2 Experimentally deformed fault rocks**

265 a. Smectite and palygorskite fault gouge material (wet deformation)

266 The examined gouge layers were recovered from the sliders. Samples retain some features related
267 to the experimental assembly such as the grooved surface of the sliders (Fig. 4a). High
268 deformation is visible towards the limit with the grooves, these type of shears have been
269 described as boundary shears. The experimentally deformed layers show microstructural features
270 previously described for clay-rich fault gouges (Rutter et al., 1986), such as P-foliation (Fig. 4b
271 and c) and R_1 shears, the deformation bands are markedly noticeable when affecting coarser
272 grains of mica and dolomite.

273 b. Sepiolite fault gouge material (wet deformation)

274 Deformation microstructures in the experimentally deformed sepiolite-rich gouge are highly
275 pronounced in mineral phases with bigger grain size, however clay mineral alignment is hard to
276 define (Fig. 5). The artificial grooves in the gouge were lost during the impregnation due to the
277 highly localized strain in the boundary shears (Fig. 5). Larger gypsum crystals are deformed in
278 domino –type asymmetric boudinage (Fig. 5b, 5c), while larger mica crystals align and delaminate
279 in favor of areas of localized shear (Fig. 5d, 5e). Dolomite crystals also appear highly fragmented
280 due to the transection of R_1 and P surfaces with trail development (Fig. 5f).

281 c. Smectite and palygorskite fault gouge material (dry deformation)

282 The experimentally deformed gouge closely resembles the deformation structures identified in
283 the natural gouge such as the R_1 shears, bands of clay minerals alternated with bands of bigger
284 grain size (Fig. 6a to 6d). A view of the shear planes shows the polished slickenside surface and
285 striae, resulting from the shear (Fig. 6e, 6f).

d. Sepiolite fault gouge material (dry deformation)

SEM examination of the deformed gouge shows similar deformation microstructures to that observed in the gouge deformed naturally and under wet conditions (Fig. 7). Being noticeable a high amount of small incipient shears that align in similar direction but are not connected between them (Fig. 7c). Figures 7d to 7f show the presence of a grid-like microfabric of the deformed gouge caused by the two main preferred orientations of sepiolite fibers. The two orientations of the fibers persist even towards the R_1 shears and on the shear planes (Fig. 7e, 7f).

4.1.3 Summary of micro-scale observations

In the naturally deformed rocks, grain orientation for the two materials studied differs significantly. The smectite- and palygorskite-rich gouge shows grain alignment with a series of parallel structures following similar orientations, on the other hand in the sepiolite-rich gouge it is noticeable the presence of two or more orientations of the fibers. Meanwhile, the differences for grain orientation identified in the two naturally deformed gouges studied remain noticeable in the experimentally deformed rocks, grain alignment in the smectite- and palygorskite-rich gouge and grid microfabric in the sepiolite-rich gouge. Finally, the presence of water during deformation does not develop any significant differences in grain orientation for either gouge, showing a similar resulting microstructure under both wet and dry conditions.

4.2 TEM observations

4.2.1 Naturally deformed fault rocks

a. Smectite and palygorskite fault rock

The gouge has a matrix mainly composed of smectite, with minor amounts of palygorskite and illite. The general texture of the rock shows phyllosilicate alignment as well as elongated porosity parallel to the basal planes of the crystals (Fig. 8a). The abundant presence of smectite helps to coat the coarse grains to maintain the fluid texture observed at lower magnification (Fig. 8b).

High-resolution images of the rock matrix in a smectite-rich area show parallel to sub-parallel lattice fringes of smectite, the (001) spacing of smectite is measured to be around 1.05 nm to 1.30 nm, due to the variable collapsing of its interlayer space in areas of poor impregnation (Fig. 8c, 8d). Lattice fringes with spacing that vary from 2.00 to 2.30 nm were also observed within the smectite-rich matrix, which might correspond to mixed layer I/S with a variable degree of collapse (Fig. 8d). The smectite crystals present broken and displaced lattice planes where the low crystallinity of the clay grains is evidenced by the absence of packets of more than two or three layers that never achieve a thickness of more than 10 nm (Fig. 8c, 8d). This kind of texture, which has been frequently described in smectites from both authigenic (Krekeler et al., 2004) and sedimentary (e.g. Nieto et al, 2016) environments, is compatible with plastic processes, able to accommodate the strain without breaking of the crystals. Illite shows lattice fringes with 1.00 nm spacing and is the most crystalline phase on the basis of Selected Area Electron Diffraction (SAED) patterns, however illite crystals are embedded in smectite crystals with a similar orientation, which hinders the chemical analysis of a single phase (Fig. 8e). HR-images show crystals with diffuse regions consistent with the polysomes structures described by Krekeler et al. (2005) (Fig. 8f).

b. Sepiolite fault rock

The general texture of the rock showed that the fibers have mainly three preferred orientations: orientations 1 and 2 have the c-axis (direction of the fiber) parallel to the imaged plane and are oriented almost perpendicular to each other; orientation 3 has the c-axis of the fibers oriented perpendicular to the imaged plane, showing a transversal section of the bundles that appear in the image as small polygons (Fig. 9). These three orientations constitute a three-dimensional grid-like microfabric of the rock. The rock matrix is composed of fiber-aggregates (bundles) with different sizes that vary from 1 μm to 100 nm (Fig. 9). The lack of fiber orientation in the rock matrix creates a large number of triangular to polygonal voids in the rock distributed throughout

the matrix (Fig. 9). SAED patterns in the matrix are difficult to obtain, however, it is possible to observe reflections representing the 110 spacing of sepiolite at around 1.23 nm (Fig. 9b inset).

FIB-cut-lamellae extracted from the red rectangle shown in Figure 3a allowed the identification of the general sense of deformation of the samples (Fig. 10a). Lamellae TEM observations show a consistent orientation for a set of feather-like structures that coincides with the general direction of shear of the sample (Fig. 10b, d and e). The feather structures show significant reduction of the grain size by bending and eventually breaking the fibers, creating an area of small oriented fibers that form the feather structure and are only recognizable at the TEM-scale (Fig. 10).

HR-TEM images show that the (110) lattice fringes in sepiolite crystals are continuous and no layer terminations were observed (Fig. 11). High-resolution images of the sepiolite crystals show lattice plane spacings that vary from 1.10 nm to 1.24 nm (Fig. 11). Some crystals (Fig. 11a) exhibit d-spacing closer to the ideal 1.20 and 1.21 nm. Meanwhile, other sepiolite crystals show progressive decrease of the d-spacing (Fig. 11b and 11c).

High-resolution images on single fibers in the naturally deformed sepiolite-rich samples showed multiple crystals with intermediate d-spacings between palygorskite and sepiolite showing a range of d-spacings from 1.03 nm to 1.18 nm (Fig. 12a). Furthermore, the images show crystals with d-spacings of 1.04 to 1.06 nm which correspond to the (110) plane of palygorskite. Crystal defects as dislocations were identified within these palygorskite crystals (Fig. 12b).

4.2.2 Experimentally deformed gouges

a. Smectite and palygorskite fault gouge material (wet and dry deformation)

Under wet conditions, low magnification images of the experimentally deformed gouge show two distinctively different textures of the rock (Fig. 13a). The first texture shows an oriented fabric constituted of laminar aggregates (Fig. 13b) that isolate the lenses of the second texture

(Fig. 13a). Smectite and illite crystals constitute the matrix of texture 1 in the artificially fabricated gouge, these phyllosilicates are aligned on their basal planes, contrary to the initial random orientation of the crushed and powdered natural rock when placed on the sliders. Smectite spacing in these samples has been identified at around 1.02 nm and it is possible to recognize a number of deformation features including delamination of the phyllosilicates and shearing of phases with larger grain size, such as gypsum (Fig. 13b).

The second texture exhibits a more homogeneous aspect without visible crystals or any particular fabric orientation (Fig. 13c). High-resolution observations show that the origin of the two textures relates to the type of phyllosilicate in the area. Texture 1 is composed of smectite and illite, while texture 2 is entirely composed of the fibrous palygorskite (Fig. 13c).

Samples deformed under the absence of water (dry deformation) show the same kind of phase segregation observed in the samples deformed under wet conditions (Fig. 14). Smectite-rich areas form sigmoidal structures and present large elongated pores that follow the orientation of the fluid-like deformation structure (Fig. 14a). SAED patterns are difficult to obtain for individual grains; however, the general SAED patterns in the matrix of both textures show significant differences confirming the segregation of mineral phases by habit. SAED pattern from areas rich in planar phyllosilicates are turbostratic, where the long axis represents d-spacings of 1.00 nm corresponding with the lattice spacing of the (001) plane of illite and possibly the collapsed smectite crystals, and the short axis represents d-spacings of 0.52 nm corresponding with the (003) plane of smectite (Fig. 14b inset).

b. Sepiolite fault gouge (wet and dry deformation)

The general texture in the gouge deformed under wet conditions shows a continuous feather structure or kinks (Fig. 15a and b). High-resolution images show (110) planes of sepiolite crystals with different d-spacing, varying from 1.14 to 1.20 nm (Fig. 15c), this particular image with angular edges is possibly viewing the crystals along the [100] direction. The parallelogram-shaped

minerals could be the result of a cross-section of rod mesocrystals that resemble open channel defects described by Krekeler and Guggenheim (2008).

Very few images were obtained from the gouge deformed under dry conditions. The lattice fringe spacing of the sepiolite crystals measured in this preparation was 1.14 nm.

4.3 Analytical Electron Microscopy

AEM analyses of single crystals from the two fault gouges in the Galera Fault Zone were collected to define the chemical compositions of sepiolite, palygorskite and smectite crystals and are presented in Figure 16 in the form of the main octahedral oxides to detect transitional compositions between sepiolite and palygorskite as well as between palygorskite and smectites. The fibrous samples plot continuously in all the compositional ranges discriminated in Suárez and García-Romero (2013), without major compositional gaps (Fig. 16). AEM analysis of smectite and palygorskite have great similitudes, palygorskite has a slightly higher Mg content than smectite, however the most significant feature to differentiate between them is their morphology.

In order to identify whether or not the origin of the smectites present within the fault plane are authigenic, 103 smectite crystals were analyzed including smectites collected from within the fault plane and smectites from the two principal lithologies in the sedimentary sequence of the wall rock. The chemical composition of the major octahedral cations in the smectite crystals are presented in Figure 17. For the full list of normalized chemical formulas see Supplementary information, Table 1.

Most of the smectites analyzed show a beidellite character. Smectites from the lutitic strata show a higher content of Fe, while those from the marly strata show a higher Al content. Smectites from the fault plane have chemical features similar to both the marls and the lutites from the

This is a preprint, the final version is subject to change, of the American Mineralogist (MSA)
Cite as Authors (Year) Title. American Mineralogist, in press.
DOI: https://doi.org/10.2138/am-2018-6316

wall rock, however their Mg content within the octahedral layer appears slightly higher than those from the wall rocks.

The identification of a small peak of palygorskite in XRD analysis (see the diffractograms of samples in Supplementary Fig. 1) motivated the exploration of the chemical composition of the sepiolite fibers in the sepiolite-rich gouge. A sequence of chemical analysis acquired within 46 individual fibers of sepiolite show small content of aluminum in 16 of the crystals. The highest Al content appears towards the edges of the crystals in 9 of the 16 crystals; while for the remaining 7 the Al content seems to be similarly distributed along the crystals. Differences in the Al content are noticeable within an individual fiber (Fig. 18), where the area of analysis 3 (in red) shows significantly higher Al content than areas 1 and 2.

4.4 Permeability

The values obtained from the permeability measurements on the smectite-rich fault gouge range between 1 $x10^{-20}$ to 1 $x10^{-21}$ m^2, which decrease almost linearly with a raise in confining pressure from 5 to 100 MPa, while results for the sepiolite-rich fault gouge range between 1 $x10^{-18}$ to 1 $x10^{-19}$ m^2 (Fig. 19).

This is a preprint, the final version is subject to change, of the American Mineralogist (MSA)
Cite as Authors (Year) Title. American Mineralogist, in press.
DOI: https://doi.org/10.2138/am-2018-6316

5. Discussion

5.1 Sepiolite to palygorskite phase transformation in the fault gouge

Sepiolite is the major phyllosilicate in the central segment of the Galera Fault (Sánchez-Roa et al., 2016), as is supported by low- and high-resolution TEM images (Figs. 9, 10, 11 and 12). Nevertheless, significant Al content has been found in various analyzed fibers, defining a continuous trend between the compositional fields of sepiolite and palygorskite (Fig. 16). This Al is preferentially associated to the border of the fibers, with a tendency to be absent in their centers (Fig. 18), and is expected to be associated to nanometer sized (less than 6 nm) discrete areas of palygorskite (Fig. 12b, 18). The d-spacing variation of lattice fringes on HR-TEM images of sepiolite ranges from 1.1 nm to 1.24 nm (Fig. 11). The presence of different d-spacings could suggest small contributions of palygorskite polysomes to the sepiolite structure (Suárez and García-Romero, 2013) that alter the regular (110) spacing of sepiolite ideally defined at 1.22 nm. The acquired images are consistent with this interpretation, however it is important to note that thickness, focus or beam damage effects could also cause alteration of regular spacings.

In nature, the progressive transformation from one phase to another, due to changes in chemical and/or physical conditions, may occur via polysomatic reactions or as growth of discrete crystals of the new phase. Polysomatic reactions are seen in the case of smectite to illite through illite/smectite mixed-layers (Hower et al., 1976), or in the case of the transformation from pyroxenes to amphiboles through pyriboles (Veblen and Buseck, 1981). In both of these cases, high-resolution images display the new polysome as individual unit cells within the former phase showing their respective characteristic spacings, which allow the clear identification of the areas in which the new polysome is present (Bozhilov et al., 2007; Vázquez et al., 2014). In other cases, the new phase nucleates as discrete crystals, sometimes assisted by topotactic or epitactic mechanisms (Sánchez-Navas, 1999), but without the existence of intermediate stages (e.g. chlorite to biotite transformation or the transformation among the aluminum silicate

polymorphs). Figure 12 could represent such a case or could be a more advanced stage in the progressive development of polysomes. Contrary to the layer silicates, the sepiolite- palygorskite polysomes would be individual chains. Considering that a lattice fringe in a high-resolution image would include at least 15 unit cells in depth, when assuming an average width of 20 nm per lath, the variability in the measured spacings could be the result of different proportions of the two types of chains, representing a weighted average of the spacings of the two polysomes. Nevertheless, we have not found individual lattice fringes corresponding to the palygorskite spacing in a matrix of sepiolite, contrary to the case described for pyriboles by Bozhilov et al. (2007). Hence, our results cannot be considered conclusive in relation to the mechanism of transformation between sepiolite and palygorskite, however chemical analysis confirms that the Al content appears often towards the edges of the crystals (Fig. 18). This suggests that the phase transformation starts affecting the edges of sepiolite fibers by including Al in palygorskite polysomes or directly producing the growth of individual crystals of palygorskite. This phenomenon in the context of fault zones can be related to fluid-rock interactions of the gouge (Sánchez-Roa et al., 2016).

5.2 Genetic relation between palygorskite and Mg-smectite in the fault gouge

Quantitative chemical analysis in palygorskite and smectite particles show a compositional overlapping between fibrous and smectite crystals (Fig. 16). This chemical similarity of some palygorskite and smectite crystals suggests that either a transformation or some mineral epitaxial overgrowth between smectite and palygorskite crystals is taking place within the smectite- and palygorskite-rich sample (Fig. 16).

To explore this possibility, AEM analysis on 103 crystals of smectite from the two main levels of the sedimentary sequence of the wall rock and smectites from the fault plane are shown in Figure 17. The results of the normalized chemical formula in the three groups of smectite show a higher interlayer Mg content for the smectites of the fault plane, but are inconclusive regarding a

change of the 2:1 layer composition of smectites. The most common products of the transformation of fibrous clay minerals in experimental studies are Mg-rich smectites (Golden and Dixon, 1990). This suggests that a portion of the smectites within the fault plane could have an authigenic origin, which would be the result of a transformation reaction from palygorskite, however the similarity of the 2:1 layer compositions between the smectites in the two contexts does not allow to either confirm nor deny such possibility.

Previous studies on the transformation of fibrous clay minerals to smectites have experimentally showed that the product of hydrothermally transformed sepiolite is often constituted by lath-like morphology smectite (Guven and Carney, 1979). This phenomenon was again observed in the transformation from palygorskite to smectite and explained by smectite forming within the palygorskite laths prior to their physical disruption producing a palygorskite pseudomorph composed of smectite (Golden and Dixon, 1990).

Based on the two well-defined textures in the experimentally deformed rock (Fig. 13, 14) and the absence of the texture segregation in the naturally deformed rock (Fig. 8), we suggest that this textural difference could be an indication that the palygorskite crystals were indeed intergrown with smectite crystals in the natural rock. Segregation of mineral phases observed in the experimentally deformed rocks can, on the other hand, occur as a result of the disaggregation of the rock during sample preparation and re-aggrupation of crystals by habit during the experiment (Fig. 13).

5.3 Deformation features in planar and fibrous clay minerals

Clay minerals are major constituents of many fault gouges (Haines and van der Pluijm, 2012; Rutter et al., 2012; Schleicher et al., 2013), reaching up to 99.5% in the Central Deforming Zone of the San Andreas Fault (Hadizadeh et al., 2012; Janssen et al., 2014), and constitute the majority of the fault gouge in the Galera Fault Zone (Sánchez-Roa et al., 2016). However, not all clay minerals have the same physical and chemical properties and possibly nor the same mode of

deformation. In this section, we aim to compare the deformation features from platy and fibrous clay minerals to identify possible differences in their behavior under shear in both natural faults and friction experiments. The Galera Fault Zone is an ideal natural example for this study due to the presence of both platy and fibrous clay minerals within its main sliding planes (Sánchez-Roa et al., 2016).

Frictional deformation in phyllosilicates is facilitated by a series of micromechanisms including grain-grain sliding when the planar minerals are aligned on their basal planes, delamination, cataclasis, crystal plasticity, and pressure-solution creep. These processes are controlled by many factors including pressure and temperature (Beeler, 2007; French et al., 2015). SEM observations on samples in this study do not show significant differences between the microstructures of wet and dry frictional experiments as has been previously described for microstructures of phyllosilicates sheared at low temperatures (Moore and Lockner, 2004; Behnsen and Faulkner, 2013; Haines et al., 2013). In general, all SEM observations in the experimentally deformed samples show distributed deformation within the phyllosilicates of the matrix (Figs. 2 to 7).

TEM observations on the smectite-rich gouge show how smectite crystals present broken and displaced lattice fringes in the rock matrix in order to accommodate deformation (Fig. 8). In this way smectite crystals ensure a uniform distribution of the shear in the rock. The quick alignment of the smectite and illite crystals of the matrix of the smectite- and palygorskite-rich samples in the experimentally deformed gouges demonstrate that when the shear deformation starts, the platy minerals rapidly adopt a preferred orientation producing a very similar fabric to the one observed in the naturally deformed rocks. Smectite crystals aggregate together with the same orientation on their basal planes, and facilitate grain on grain sliding as well as delamination processes that accommodate deformation through creeping (Fig. 8).

On the other hand, the fibrous phyllosilicate gouge shows mainly three different orientations of the fibers. This grid-like microfabric (Fig. 9) and the absence of weak cleavage planes for

intragranular sliding result in the formation of feather structures that mark areas where the deformation processes have been localized producing the observed grain size reduction through a mechanical bending and breaking of the fibers. The orientation of the feather-like structures (Fig. 10), resemble the orientation of Riedel shears (Rutter et al., 1986). Indicating that deformation is localizing by bending and breaking the fibers at a very small scale that is not visible until the clay fraction of the gouge is examined in detail (Fig. 10, 15).

In the case of the experimentally deformed smectite- and palygorskite-rich gouge no feather structures were observed, a phenomenon that can be explained by the high amount of smectite in the sample that accommodates most of the deformation without the need to affect the stronger palygorskite-rich areas.

In HR-TEM observations, the delamination processes are visible in the smectite crystals, however in the fibrous materials the lattice fringes appear continuous. The higher strength of the fibrous structure hinders delamination processes accommodating the imposed deformation by breaking and bending of fibers resulting in a series of feather-like structures at the micro-scale (Fig. 10).

5.4 Geological implications

Based on our results, we propose that the mineral transformations in the Mg-rich fault gouges of the Galera Fault are a consequence of the fluid depletion in Mg with progressive exhumation and a proportional increase of Al content enhanced by the interaction with the Al-rich wall rocks. Sánchez-Roa et al. (2016) showed that mineralogical and geochemical differences between fault gouges and wall rocks are likely to be the result of periods of fluid-rock interaction within the Galera Fault. MgO and As gains in fault gouges pointed to a circulation of hot deep fluids as the source of the Mg-rich fluid, produced by the dissolution of the thick dolostone sequences that form the Mesozoic carbonatic basement. Sepiolite precipitated directly from a Mg-rich fluid while palygorskite and smectite formation could be products of the interaction of the fluid with

548 the Al-rich host rock and the infiltration of oxidized basinal fluids with high pH^+. The evolution
549 sequence identified in this study starts with the precipitation of sepiolite from Mg-rich
550 hydrothermal fluids (Sánchez-Roa et al., 2016). Sepiolite crystals start to incorporate palygorskite
551 domains to produce a first evolution stage where both sepiolite and palygorskite are present as
552 independent crystals as is the case of the studied gouge from the Galera Fault. Following this, we
553 propose a second evolution stage intermediate between the two gouges studied, in which all
554 sepiolite has been transformed to palygorskite. The smectite-palygorskite gouge from the Galera
555 Fault constitutes a third stage of transformation, in which the smectites in the wall rock change
556 their interlayer composition and a part of the palygorskite could have been transformed to
557 smectite as a result of the large Al-availability forming Mg-rich smectite. In a more advanced
558 stage, it is possible that further alteration of the fault gouge results in a platy Mg-rich smectite
559 enrichment, which could alter fault strength and permeability, affecting earthquake nucleation
560 and propagation processes.

561 The permeability of fault zones is a relevant property that controls the subsurface fluid flow and
562 plays an important role in coseismic fluid pressure changes, pore pressure build-ups and
563 potential weakening of faults (Scuderi and Collettini, 2016; Faulkner et al., 2018). There is a
564 difference of almost two orders of magnitude in the measured permeability for the two fault
565 gouges in this study (Fig. 19). This permeability contrast can be related to the dominant
566 phyllosilicate for each gouge. Both gouges decrease their permeability with increasing confining
567 pressure, however the smectite-rich fault gouge sustains greater decline in permeability for a
568 given change in confining pressure (Fig. 19). The faster decrease in permeability for the smectite-
569 gouge can be related to a much higher level of sheet alignment and lateral connectivity of the
570 platy smectite crystals at medium to high pressures facilitated by the high particle mobility of this
571 mineral (Behnsen and Faulkner, 2011). On the other hand, the grid-like microfabric in the fully
572 fibrous material can leave room for a higher number of interconnected pores due to the lack of
573 fiber alignment that adds to the structural microporosity of the fibers, as a consequence of their

574 internal channels. These results show how the permeability of the gouges in the Galera Fault is
575 strongly affected by the mineralogy of the gouge, implying that mineral authigenic growth and
576 mineral transformations could constitute a controlling factor on the permeability of the fault
577 zone.

578 The strength of the two fault gouges in the Galera Fault show highly contrasting values, the
579 sepiolite-rich gouge has a higher friction coefficient (μ=0.47 under wet deformation), while the
580 smectite and palygorskite-rich gouge has a significantly lower friction coefficient (μ=0.17 under
581 wet deformation) (Sánchez-Roa et al., 2016). The presence of smectite has proven to have
582 important effects on the strength of faults by contributing to a lower frictional strength and has
583 been reported to have a weakening effect on concentrations as low as 10 wt% (Oohashi et al.,
584 2015). Furthermore, previous studies comparing the strength of monomineralic fibrous clay
585 minerals and the smectite saponite have shown that their frictional strength is dictated by their
586 crystal structure showing that fibrous Mg-rich phyllosilicates are stronger than the platy smectite
587 (Sánchez-Roa et al., 2017). Therefore, we suggest that the strength of the Galera Fault could be
588 significantly controlled by the palygorskite to smectite ratio within the fault planes.

589 Mineral transformations between fibrous and planar clay minerals (specifically smectite) could
590 occur in a variety of geological settings involving Mg-rich environments. As a consequence, these
591 mineral transformations will considerably change important chemical and physical properties,
592 such as surface area and cation exchange capacity that significantly alter the microfabric,
593 permeability and strength of the geological material.

594

595 Acknowledgments

596 The authors would like to thank Dr. M.M. Abad-Ortega, A. Martinez-Morales, Dr. M. A.
597 Laguna, Dr. A. Ibarra and Dr. R. Fernández-Pacheco for their support in electron microscopy

598 data acquisition. The authors thank the reviewers E. García-Romero and M. Krekeler for their
599 comments that led to significant improvements. This work has been financed by the research
600 projects CGL2011-30153-C02-01, CGL2011-30153- C02-02, and CGL2013-46169-C2-1-P from
601 MINECO, research project UJA2014/06/17 from the Universidad-Caja Rural de Jaén, Research
602 Groups RNM-179 and RNM-325 of the Junta de Andalucía, UK NERC grant NE/J024449/1
603 and the F.P.I. Grant No. BES-2012-052 562 from the Spanish Government (Ministerio de
604 Economía y Competitividad).

605 References

606 Abad, I., Nieto, F., and Velilla, N., 2002, Chemical and textural characterisation of diagenetic to
607 low-grade metamorphic phyllosilicates in turbidite sandstones of the South Portuguese
608 Zone: A comparison between metapelites and sandstones: Schweizerische Mineralogische
609 und Petrographische Mitteilungen, v. 82, p. 303–324.

610 Beeler, N.M., 2007, Laboratory-observed faulting in Intrinsically and Apparently Weak Materials:
611 The Seismogenic Zone of Subduction Thrust Faults, p. 370–449.

612 Behnsen, J., and Faulkner, D.R., 2013, Permeability and frictional strength of cation-exchanged
613 montmorillonite: Journal of Geophysical Research: Solid Earth, v. 118, no. 6, p. 2788–2798,
614 doi: 10.1002/jgrb.50226.

615 Behnsen, J., and Faulkner, D.R., 2011, Water and argon permeability of phyllosilicate powders
616 under medium to high pressure: Journal of Geophysical Research: Solid Earth, v. 116, no.
617 12, p. 1–13, doi: 10.1029/2011JB008600.

618 Bozhilov, K.N., Brownstein, D., and Jenkins, D.M., 2007, Biopyribole evolution during tremolite
619 synthesis from dolomite and quartz in CO2-H2O fluid: American Mineralogist, v. 92, no. 5-
620 6, p. 898–908, doi: 10.2138/am.2007.2376.

Brace, W.F., Walsh, J.B., and Frangos, W.T., 1968, Permeability of Granite under High Pressure: Journal of Geophysical Research, v. 73, no. 6.

Cliff, G. and Lorimer, G. W., 1975, The quantitative analysis of thin specimens: Journal of Microscopy, 103: 203-207. doi:10.1111/j.1365-2818.1975.tb03895.x

Cox, S.F., Knackstedt, M.A., and Braun, J., 2001, Principles of structural control on permeability and fluid flow in hydrothermal systems: Reviews in Economic Geology, v. 14, p. 1–24.

Faulkner, D.R., Jackson, C.A.L., Lunn, R.J., Schlische, R.W., Shipton, Z.K., Wibberley, C.A.J., and Withjack, M.O., 2010, A review of recent developments concerning the structure, mechanics and fluid flow properties of fault zones: Journal of Structural Geology, v. 32, no. 11, p. 1557–1575, doi: 10.1016/j.jsg.2010.06.009.

Faulkner, D.R., Sánchez-Roa, C., Boulton, C., and den Hartog, S.A.M., Pore Fluid Pressure Development in Compacting Fault Gouge in Theory, Experiments, and Nature: Journal of Geophysical Research: Solid Earth, 123. https://doi.org/10.1002/2017JB015130

French, M.E., Chester, F.M., and Chester, J.S., 2015, Micromechanisms of creep in clay-rich gouge from the Central Deforming Zone of the San Andreas Fault: Journal of Geophysical Research B: Solid Earth, v. 120, no. 2, p. 827–849, doi: 10.1002/2014JB011496.

García-Romero, E., and Suárez, M., 2010, On the chemical composition of sepiolite and palygorskite: Clays and Clay Minerals, v. 58, no. 1, p. 1–20, doi: 10.1346/CCMN.2010.0580101.

García-Romero, E., and Suárez, M., 2013, Sepiolite-palygorskite: Textural study and genetic considerations: Applied Clay Science, doi: 10.1016/j.clay.2013.09.013.

García-Tortosa, F.J., Alfaro, P., Sanz de Galdeano, C., and Galindo-Zaldívar, J., 2011, Glacis geometry as a geomorphic marker of recent tectonics: The Guadix-Baza basin (South Spain): Geomorphology, v. 125, no. 4, p. 517–529, doi: 10.1016/j.geomorph.2010.10.021.

Giese, R.F., 1978, Electrostatic Interlayer Forces of Layer Structure Minerals.: Clays and Clay Minerals, v. 26, no. 1, p. 51–57, doi: 10.1346/CCMN.1978.0260106.

Golden, D.C., and Dixon, J.B., 1990, Low-temperature alteration of palygorskite to smectite: v. 38, no. 4, p. 401–408.

Guven, N., and Carney, L.L., 1979, Hydrothermal Transformation of Sepiolite to Stevensite and The Effect of Added Chlorides and Hydroxides.: Clays and Clay Minerals, v. 27, no. 4, p. 253–260, doi: 10.1346/CCMN.1979.0270403.

Hadizadeh, J., Mittempergher, S., Gratier, J.P., Renard, F., Di Toro, G., Richard, J., and Babaie, H. a., 2012, A microstructural study of fault rocks from the SAFOD: Implications for the deformation mechanisms and strength of the creeping segment of the San Andreas Fault: Journal of Structural Geology, v. 42, p. 246–260, doi: 10.1016/j.jsg.2012.04.011.

Haines, S.H., Kaproth, B., Marone, C., Saffer, D., and Van der Pluijm, B., 2013, Shear zones in clay-rich fault gouge: A laboratory study of fabric development and evolution: Journal of Structural Geology, v. 51, p. 206–225, doi: 10.1016/j.jsg.2013.01.002.

Haines, S.H., and van der Pluijm, B.A., 2012, Patterns of mineral transformations in clay gouge, with examples from low-angle normal fault rocks in the western USA: Journal of Structural Geology, v. 43, p. 2–32, doi: 10.1016/j.jsg.2012.05.004.

Hickman, S., Sibson, R., and Bruhn, R., 1995, Mechanical involvement of fluids in faulting: Journal of Geophysical Research, v. 100, no. B7, p. 12831–12840, doi: 10.1029/94EO01059.

Houwers, M.E., Heijnen, L.J., Becker, A., and Rijkers, R., 2015, A Workflow for the Estimation of Fault Zone Permeability for Geothermal Production A General Model Applied on the Roer Valley Graben in the Netherlands: Proceedings World Geothermal Congress 2015, , no. April, p. 9.

Hower, J., Eslinger, E. V., Hower, M.E., and Perry, E. a., 1976, Mechanism of burial metamorphism of argillaceos sediment: Geological Society Of America Bulletin, v. 87, no. 60512, p. 725–737, doi: 10.1130/0016-7606(1976)87<725.

Ibanez, W.D., and Kronenberg, A.K., 1993, Experimental deformation of shale: Mechanical properties and microstructural indicators of mechanisms: International Journal of Rock Mechanics and Mining Sciences and, v. 30, no. 7, p. 723–734, doi: 10.1016/0148-9062(93)90014-5.

Janssen, C., Wirth, R., Wenk, H.R., Morales, L., Naumann, R., Kienast, M., Song, S.R., and Dresen, G., 2014, Faulting processes in active faults - Evidences from TCDP and SAFOD drill core samples: Journal of Structural Geology, v. 65, p. 100–116, doi: 10.1016/j.jsg.2014.04.004.

Kim, J.W., Peacor, D.R., Tessier, D., and Elsass, F., 1995, A technique for maintaining texture and permanent expansion of smectite interlayers for TEM observations: Clays and Clay Minerals, v. 43, no. 1, p. 51–57, doi: 10.1346/CCMN.1995.0430106.

683 Krekeler, M.P.S., Guggenheim, S., Rakovan, J., 2004, A microtexture study of palygorskite-rich
684 sediments from the Hawthorne Formation, Southern Georgia, by transmission electron microscopy and
685 atomic force microscopy. Clays and Clay Minerals, v. 52, no. 3, p. 263–274.

686 Krekeler, M.P.S., Hammerly, E., Rakovan, J., Guggenheim, S., 2005, Microscopy studies of the
687 palygorskite to smectite transformation. Clays and Clay Minerals, 53, 94–101.

688 Krekeler, M.P.S., and Guggenheim, S., 2008, Defects in microstructure in palygorskite-sepiolite
689 minerals: A transmission electron microscopy (TEM) study: Applied Clay Science, v. 39, no.
690 1-2, p. 98–105, doi: 10.1016/j.clay.2007.05.001.

691 Logan, J.M., Friedman, M., Higgs, N., Dengo, C., and Shimamoto, T., 1979, Experimental
692 studies of simulated gouge and their application to studies of natural fault zones: Proc.
693 Conf. VIII - Analysis of Actual Fault Zones in Bedrock, p. 305–343.

694 Mares, V.M., and Kronenberg, a. K., 1993, Experimental deformation of muscovite: Journal of
695 Structural Geology, v. 15, no. 9-10, p. 1061–1075, doi: 10.1016/0191-8141(93)90156-5.

696 Mitchell, T.M., and Faulkner, D.R., 2008, Experimental measurements of permeability evolution
697 during triaxial compression of initially intact crystalline rocks and implications for fluid flow
698 in fault zones: Journal of Geophysical Research: Solid Earth, v. 113, no. 11, p. 1–16, doi:
699 10.1029/2008JB005588.

700 Moore, D.E., and Lockner, D.A., 2004, Crystallographic controls on the frictional behavior of
701 dry and water-saturated sheet structure minerals: Journal of Geophysical Research, v. 109,
702 no. B03401, p. 1–16, doi: 10.1029/2003JB002582.

703 Nieto, F., Arroyo, X., Aróstegui, J., 2016, XRD-TEM-AEM comparative study of *n*-
704 alkylammonium smectites and interstratified minerals in shallow-diagenetic carbonate

sediments of the Basque-Cantabrian Basin: American Mineralogist, v. 101, p. 385–398, doi: https://doi.org/10.2138/am-2016-5301.

Oohashi, K., Hirose, T., Takahashi, M., and Tanikawa, W., 2015, Dynamic weakening of smectite-bearing faults at intermediate velocities: Implications for subduction zone earthquakes: Journal of Geophysical Research-Solid Earth, v. 120, p. 11881, doi: 10.1002/2015JB011881.Received.

Overwijk, M.H.F., 1993, Novel scheme for the preparation of transmission electron microscopy specimens with a focused ion beam: Journal of Vacuum Science & Technology B: Microelectronics and Nanometer Structures, v. 11, no. 6, p. 2021–2024, doi: 10.1116/1.586537.

Peacor, D.R., 1992, Analytical electron microscopy, *in* Buseck, P.R. ed., Minerals and reactions at the atomic scale: Transmission electron microscopy., Mineralogical Society of America, p. 113–140.

Rutter, E.H., Faulkner, D.R., and Burgess, R., 2012, Structure and geological history of the Carboneras Fault Zone, SE Spain: Part of a stretching transform fault system: Journal of Structural Geology, v. 45, p. 68–86, doi: 10.1016/j.jsg.2012.08.009.

Rutter, E.H., Maddock, R.H., Hall, S.H., and White, S.H., 1986, Comparative microstructures of natural and experimentally produced clay-bearing fault gouges: Pure and Applied Geophysics, v. 124, no. 1-2, p. 3–30, doi: 10.1007/BF00875717.

Sakuma, H., and Suehara, S., 2015, Interlayer bonding energy of layered minerals: Implication for the relationship with friction coefficient: Journal of Geophysical Research: Solid Earth, p. 2212–2219, doi: 10.1002/2015JB011900.

727 Sánchez-Navas, A., 1999, Sequential kinetics of a muscovite-out reaction: A natural example:
728 American Mineralogist, v. 84, no. 9, p. 1270–1286.

729 Sánchez-Navas, A., and Galindo-Zaldívar, J., 1993, Alteration and deformation microstructures
730 of biotite from plagioclase-rich dykes (Ronda Massif, S. Spain): European Journal of
731 Mineralogy, v. 5, no. 1987, p. 245–256.

732 Sánchez-Roa, C., Jiménez-Millán, J., Abad, I., Faulkner, D.R., Nieto, F., and García-Tortosa, F.J.,
733 2016, Fibrous clay mineral authigenesis induced by fluid-rock interaction in the Galera fault
734 zone (Betic Cordillera, SE Spain) and its influence on fault gouge frictional properties:
735 Applied Clay Science, doi: 10.1016/j.clay.2016.06.023.

736 Sánchez-Roa, C., Faulkner, D.R., Boulton, C., Jimenez-Millan, J., Nieto, 2017, How phyllosilicate
737 mineral structure affects fault strength in Mg-rich fault systems: Geophysical Research
738 Letters, doi:

739 Schleicher, A.M., Hofmann, H., and van der Pluijm, B.A., 2013, Constraining clay hydration state
740 and its role in active fault systems: Geochemistry, Geophysics, Geosystems, v. 14, no. 4, p.
741 1039–1052, doi: 10.1002/ggge.20077.

742 Schleicher, A.M., Van Der Pluijm, B. a., Solum, J.G., and Warr, L.N., 2006, Origin and
743 significance of clay-coated fractures in mudrock fragments of the SAFOD borehole
744 (Parkfield, California): Geophysical Research Letters, v. 33, no. 16, doi:
745 10.1029/2006GL026505.

746 Schleicher, A.M., van der Pluijm, B.A., and Warr, L.N., 2012, Chlorite-smectite clay minerals and
747 fault behavior: New evidence from the San Andreas Fault Observatory at Depth (SAFOD)
748 core: Lithosphere, v. 4, no. 3, p. 209–220, doi: 10.1130/L158.1.

749 Scuderi, M.M., and Collettini, C., 2016, The role of fluid pressure in induced vs. triggered
750 seismicity: insights from rock deformation experiments on carbonates.: Scientific reports, v.
751 6, no. April, p. 24852, doi: 10.1038/srep24852.

752 Sibson, R.H., White, S.H., and Atkinson, B.K., 1979, Fault rock distribution and structure within
753 the Alpine Fault Zone: a preliminary account, in The Origin of the Southern Alps, R. I.
754 Walcott and M. M. Cresswell (Editors), R. Soc. New Zealand Bull. 18, 55–65.

755 Suárez, M., and García-Romero, E., 2013, Sepiolite–palygorskite: a continuous polysomatic
756 series. Clays Clay Miner. 61, 5, 461–472.

757 Van der Pluijm, B., Lee, J., and Peacor, D.R., 1988, Analytical Electron Microscopy and the
758 Problem of Potassium Diffusion: Clays and Clay Minerals, v. 36, no. 6, p. 498–504.

759 Vázquez, M., Nieto, F., Morata, D., Droguett, B., Carrillo-Rosua, F.J., and Morales, S., 2014,
760 Evolution of clay mineral assemblages in the Tinguiririca geothermal field, Andean
761 Cordillera of central Chile: an XRD and HRTEM-AEM study: Journal of Volcanology and
762 Geothermal Research, v. 282, p. 43–59, doi: 10.1016/j.jvolgeores.2014.05.022.

763 Veblen, D.R., and Buseck, P.R., 1981, Hydrous pyriboles and sheet silicates in pyroxenes and
764 uralites: intergrowth microstructures and reaction mechanisms.: American Mineralogist, v.
765 66, no. 11-12, p. 1107–1134.

766 Whitney, D.L., and Evans, B.W., 2010, Abbreviations for names of rock-forming minerals.
767 American Mineralogist, 95, 185–187.

Figure Captions

Figure 1. Geological map of the Galera Fault, modified from García-Tortosa et al. (2011). I: Sampling site by the Galera Village, Smectite- and palygorskite-rich fault gouge II: Sampling site Rambla de los Pilares, Sepiolite-rich fault gouge.

Figure 2. BSE image showing the deformation features of the naturally deformed smectite and palygorskite fault gouge, including P-foliation following the alignment of platy clay minerals, R_1 (Riedel) shears transecting the P-foliation, and Y surfaces parallel to the shear zone. Mineral abbreviations acording to Whitney and Evans (2010), Or: orthoclase, Dol: dolomite, Qz: quartz.

Figure 3. a. BSE image showing the deformation features of the naturally deformed sepiolite fault gouge and deformation in larger grains of mica and dolomite. The red rectangle indicates the area selected for FIB-SEM lamellae extraction for TEM analysis **b**. Secondary electron image (in-lens detector) of the matrix of the rock showing the fibrous character of sepiolite.

Figure 4. a. BSE image of the experimentally deformed smectite and palygorskite fault gouge material under wet deformation**. b.** Enlarged view of the R_1 shear and P-foliation. **c.** Enlarged view of the P-foliation and alignment of dolomite and orthoclase grains.

Figure 5. a. BSE image of the experimentally deformed sepiolite fault gouge material under wet deformation. Shear direction indicated with half arrows. **b.** Enlargement of a boudinage structure on a gypsum crystal. **c** Enlargement of R_1 shear. Shear direction indicated with half arrows. d **to f.** Enlargement of structural features in the sample.

Figure 6. **a.** BSE image of the experimentally deformed smectite and palygorskite fault gouge material under dry deformation. **b, c, and d.** Enlargement of structural features in the sample. The red rectangle indicates the area selected for FIB-SEM lamellae extraction for TEM analysis

790 **e.** and **f.** Secondary electrons image of the shear planes after deformation with horizontal striae
791 and polished slickenside surface.

792 **Figure 7. a.** BSE image of the experimentally deformed sepiolite fault gouge material under dry
793 deformation. **b and c.** Enlargement of structural features in the sample. The red parallelogram
794 indicates the site selected for FIB-SEM extraction for TEM analysis. **d.** Secondary electrons
795 high-magnification image (in-lens detector) showing sepiolite crystals of the matrix **e.** and **f.**
796 Secondary electrons image of the shear planes after deformation under dry conditions.

797 **Figure 8. a.** TEM image showing the general texture of the naturally deformed smectite and
798 palygorskite fault rock. **b.** Smectite crystals coating coarse dolomite grain. **c.** High-resolution
799 image of smectite crystals showing broken and displaced lattice fringes. **d.** Smectite-rich matrix
800 shows smectite crystals with (001) spacing of 1.30 nm, and an area of unidentified phases with
801 lattice fringes spaced 2.00 to 2.30 nm. **e.** HR-image of the matrix of the rock showing the
802 proximity of the smectite and illite crystals. **f.** HR-image of crystals with discontinuous lattice
803 fringes of variable d-spacing ranging from 1.9 to 2.4 nm. Mineral abbreviations acording to
804 Whitney and Evans (2010), Ilt: illite, Dol: dolomite, Sme: smectite.

805 **Figure 9.** TEM images from a Cu-washer of the sepiolite fault rock. **a.** General fabric on the
806 rock with variable rod sizes. **b.** Image of the rock matrix showing the disorientation of sepiolite
807 fibers. Inset: SAED pattern on the rock matrix. Mineral abbreviations acording to Whitney and
808 Evans (2010), Sep: sepiolite.

809 **Figure 10.** TEM images of a FIB-lamellae sample of a sepiolite fault rock **a.** General view of the
810 lamellae extracted from the red rectangle shown in Fig. 3a. Small letters show the position of
811 subfigures b, d and e whitin the extracted FIB-lamellae. Arrows indicate the direction of shear. **b.**
812 Feather structure following the direction of shear. **c.** General texture of the naturally deformed

sepiolite-rich fault rock. **d. and e.** Feather structures. Mineral abbreviations acording to Whitney and Evans (2010), Sep: sepiolite.

Figure 11. a. High-resolution TEM image of the sepiolite crystal lattice with close to ideal d-spacing 1.21 nm. Insets show the intensity profiles along crystals A and B and average d-spacing results. **b and c.** High-resolution images of the sepiolite crystal lattice with variable d-spacing from 1.10 nm to 1.24 nm. Mineral abbreviations acording to Whitney and Evans (2010), Sep: sepiolite.

Figure 12. HR-TEM images of individual fibers in the sepiolite-rich gouge. **a.** Fibers with lattice spacing of 1.18 nm, slightly lower to those for ideal sepiolite. **b.** Fiber with lattice spacings corresponding with a palygorskite crystal.

Figure 13. a. Low magnification image of the experimentally deformed smectite and palygorskite gouge exhibiting two distinctively different textures of the rock. **b.** Magnification of texture 1 showing aggregates of smectite crystals. **c.** Magnification of texture 2 showing disoriented palygorskite fibers. Mineral abbreviations acording to Whitney and Evans (2010), Gp: gypsum, Ilt: illite, Pal: palygorskite, Sme: smectite.

Figure 14. a. TEM image and general view of the lamellae extracted from the red rectangle shown in Fig. 7c **b.** Magnification of texture 1 showing aggregates of smectite crystals. **inset.** SAED patterns of texture 1. c. Magnification of texture 2 showing disoriented palygorskite fibers. **inset.** SAED patterns of texture 2. Mineral abbreviations acording to Whitney and Evans (2010), Pal: palygorskite, Sme: smectite.

Figure 15. a. Low magnification TEM image showing the general texture of the sepiolite fault gouge under wet deformation and kinked sepiolite laths **b.** TEM image on the feather-like structures that form the matrix after deformation **c.** HR-TEM image of sepiolite crystals in the sepiolite fault gouge material under wet deformation. Mineral abbreviations acording to Whitney and Evans (2010), Sep: sepiolite.

838 **Figure 16.** Variability in the octahedral cation content of the sepiolites, palygorskites and
839 smectites of the study and their chemical classification according to Suárez and García-Romero
840 (2013). Ideal octahedral cation oxide content for sepiolite and palygorskite are plotted according
841 to García-Romero and Suárez (2010).

842 **Figure 17.** Ternary plot of major octahedral cations in smectite crystals from the fault rock in
843 blue, lutitic wall rock in red and marly wall rock in green. Yellow and light-blue squares
844 correspond to smectite crystals from the fault plane analysed after homoionization with K and
845 Ca respectevly.

846 **Figure 18. a.** Sepiolite crystal and selected areas for microanalysis **b.** TEM-AEM analysis of
847 three selected areas of sepiolite crystal.

848 **Figure 19.** Permeability measurements on the two gouges with increasing confining pressure on
849 a triaxial deformation apparatus.

850

851

Supplementary Material

Supplementary Table 1. Structural formulas calculated from AEM data for smectites normalized to $O_{10}(OH)_2$. All Fe as Fe^{3+} and $^{IV}Al = (4 - Si)$.

		Sample	Formula										
			Si	AlIV	AlVI	Fe	Mg (oct)	∑ oct.	Ca	K	Na	Mg (inter)	∑ inter.
Untreated samples	Fault gouge	1 GP-3-1	3.890	0.110	0.752	0.563	0.685	2.000	0.000	0.299	0.000	0.248	0.547
		2 GP-3-3	3.913	0.087	0.918	0.529	0.553	2.000	0.000	0.264	0.000	0.187	0.452
		3 GP-3-4	3.844	0.156	1.225	0.384	0.391	2.000	0.017	0.384	0.000	0.064	0.465
		4 GP-3-5	3.896	0.104	1.374	0.278	0.348	2.000	0.035	0.313	0.000	0.035	0.383
		5 GP-3-6	3.757	0.243	1.409	0.313	0.278	2.000	0.087	0.313	0.000	0.017	0.417
		6 GP-3-7	3.786	0.214	1.391	0.331	0.278	2.000	0.052	0.314	0.000	0.036	0.403
		7 GP-3-8	3.956	0.044	1.240	0.295	0.465	2.000	0.104	0.260	0.000	0.021	0.385
		8 GP-3-9	3.806	0.194	1.092	0.539	0.370	2.000	0.000	0.156	0.000	0.204	0.360
		9 GP-3-10	3.783	0.217	1.038	0.540	0.422	2.000	0.087	0.192	0.000	0.136	0.415
		10 GP-3-11	3.876	0.124	1.011	0.541	0.419	1.971	0.157	0.314	0.000	0.000	0.471
		11 GP-3-12	3.865	0.135	1.159	0.385	0.000	1.544	0.192	0.420	0.000	0.000	0.612
		12 GP-3-13	3.984	0.016	1.180	0.398	0.422	2.000	0.069	0.139	0.000	0.080	0.288
		13 GP-3-14	3.716	0.284	1.329	0.280	0.390	2.000	0.053	0.333	0.000	0.118	0.504
		14 GP-3-15	3.708	0.292	1.113	0.492	0.395	2.000	0.053	0.457	0.000	0.062	0.572
		15 GP-3-16	3.728	0.272	1.260	0.401	0.339	2.000	0.070	0.279	0.000	0.097	0.445
		16 GP-3-17	3.780	0.220	1.181	0.473	0.347	2.000	0.035	0.385	0.000	0.056	0.476
		17 GP-3-18	3.869	0.131	1.118	0.503	0.379	2.000	0.000	0.260	0.000	0.125	0.385
		18 GP-3-19	3.997	0.003	1.057	0.365	0.578	2.000	0.035	0.174	0.000	0.169	0.378
		19 GP-3-20	3.754	0.246	1.256	0.419	0.325	2.000	0.017	0.384	0.000	0.076	0.478
		20 GP-3-21	3.874	0.126	1.049	0.491	0.461	2.000	0.000	0.456	0.000	0.065	0.521
		21 GP-3-22	4.005	0.000	1.214	0.312	0.474	2.000	0.000	0.191	0.000	0.132	0.323
		22 GP-3-23	3.841	0.159	1.133	0.402	0.465	2.000	0.122	0.297	0.000	0.041	0.460
		23 GP-3-24	3.755	0.245	1.095	0.511	0.388	1.994	0.071	0.511	0.000	0.000	0.582
		24 GP-3-25	3.830	0.170	1.124	0.455	0.421	2.000	0.052	0.280	0.000	0.103	0.436
		25 GP-3-26	3.673	0.327	1.307	0.334	0.359	2.000	0.070	0.387	0.000	0.080	0.537
		26 GP-3-1	3.904	0.096	1.153	0.416	0.431	2.000	0.069	0.208	0.000	0.090	0.368
		27 GP-3-2	3.860	0.140	1.088	0.421	0.491	2.000	0.070	0.491	0.000	0.000	0.561
		28 GP-3-3	3.880	0.120	0.989	0.589	0.422	2.000	0.000	0.139	0.000	0.202	0.340
		29 GP-3-4	4.071	0.000	0.699	0.437	0.864	2.000	0.000	0.175	0.000	0.202	0.376
		30 GP-3-5	3.841	0.159	1.221	0.279	0.500	2.000	0.000	0.192	0.000	0.233	0.425
		31 GP-3-6	3.606	0.394	1.452	0.261	0.287	2.000	0.035	0.279	0.000	0.166	0.480
		32 GP-3-7	4.033	0.000	1.004	0.589	0.398	1.991	0.000	0.294	0.000	0.000	0.294
		33 GP-3-8	3.759	0.241	1.187	0.400	0.413	2.000	0.000	0.191	0.000	0.231	0.422
		34 GP-3-9	3.724	0.276	1.595	0.225	0.180	2.000	0.052	0.191	0.000	0.080	0.323
		35 GP-3-10	3.979	0.021	1.283	0.191	0.526	2.000	0.000	0.174	0.000	0.186	0.360
		36 GP-3-1	3.783	0.217	1.317	0.331	0.352	2.000	0.035	0.331	0.000	0.084	0.450
		37 GP-3-2	3.534	0.466	1.390	0.247	0.000	1.637	0.247	0.495	0.000	0.000	0.742
		38 GP-3-3	3.722	0.278	1.242	0.454	0.303	2.000	0.035	0.315	0.000	0.098	0.448
		39 GP-3-4	3.701	0.299	1.509	0.362	0.130	2.000	0.017	0.034	0.000	0.180	0.232
		40 GP-3-5	3.834	0.166	1.344	0.278	0.379	2.000	0.000	0.156	0.000	0.194	0.350
		41 GP-3-6	3.690	0.310	1.386	0.367	0.246	2.000	0.000	0.455	0.000	0.051	0.506
		42 GP-3-7	3.751	0.249	1.077	0.576	0.347	2.000	0.000	0.244	0.000	0.176	0.420
		43 GP-3-8	3.919	0.081	1.201	0.369	0.404	1.974	0.000	0.562	0.000	0.000	0.562
		44 GP-3-9	3.919	0.081	1.121	0.435	0.443	2.000	0.000	0.366	0.000	0.079	0.445
		45 GP-3-10	3.847	0.153	1.204	0.383	0.413	2.000	0.000	0.278	0.000	0.144	0.422
		46 GP-3-11	3.861	0.139	1.339	0.296	0.365	2.000	0.035	0.330	0.000	0.052	0.417
	Lutites	47 GP-12-1	3.931	0.069	0.845	0.776	0.379	2.000	0.017	0.103	0.000	0.155	0.276
		48 GP-12-2	3.670	0.330	0.945	0.681	0.373	2.000	0.000	0.262	0.000	0.221	0.483
		49 GP-12-3	3.699	0.301	1.154	0.508	0.338	2.000	0.035	0.438	0.000	0.065	0.539
		50 GP-12-4	3.652	0.348	1.470	0.346	0.184	2.000	0.017	0.104	0.000	0.197	0.318
		51 GP-12-5	4.016	0.000	1.339	0.343	0.318	2.000	0.000	0.103	0.000	0.076	0.179
		52 GP-12-6	4.005	0.000	1.238	0.447	0.316	2.000	0.017	0.069	0.000	0.097	0.183
		53 GP-12-7	4.009	0.000	1.106	0.449	0.445	2.000	0.000	0.121	0.000	0.143	0.264
		54 GP-12-8	4.003	0.000	0.853	0.453	0.661	1.967	0.331	0.087	0.000	0.000	0.418
		55 GP-12-9	3.981	0.019	1.371	0.395	0.234	2.000	0.000	0.069	0.000	0.092	0.161
		56 GP-12-10	3.748	0.252	1.205	0.468	0.326	2.000	0.000	0.121	0.000	0.229	0.350
		57 GP12-2	3.924	0.076	0.792	0.799	0.409	2.000	0.000	0.226	0.000	0.129	0.355
		58 GP12-3	3.488	0.512	1.578	0.397	0.025	2.000	0.000	0.035	0.000	0.251	0.286
		59 GP12-4	3.806	0.194	0.935	0.712	0.352	2.000	0.000	0.139	0.000	0.204	0.343
		60 GP12-5	3.879	0.121	1.259	0.552	0.190	2.000	0.000	0.172	0.000	0.069	0.241
		61 GP12-6	3.941	0.059	1.055	0.720	0.226	2.000	0.000	0.051	0.000	0.117	0.168
		62 GP12-7	3.809	0.191	0.939	0.748	0.313	2.000	0.017	0.191	0.000	0.139	0.348
		63 GP12-8	3.826	0.174	0.835	0.730	0.435	2.000	0.000	0.122	0.000	0.243	0.365
		64 GP12-9	3.618	0.382	1.574	0.329	0.098	2.000	0.035	0.087	0.000	0.162	0.283
		65 GP12-10	4.031	0.000	1.223	0.431	0.346	2.000	0.000	0.155	0.000	0.033	0.188

857

	Marls	66	GP1-2	3.873	0.127	1.234	0.436	0.330	2.000	0.035	0.349	0.000	0.019	0.403
		67	GP1-3	3.644	0.356	1.587	0.226	0.188	2.000	0.035	0.156	0.000	0.159	0.350
		68	GP1-4	3.725	0.275	1.604	0.191	0.204	2.000	0.052	0.296	0.000	0.040	0.388
		69	GP1-5	3.550	0.450	1.614	0.192	0.194	2.000	0.052	0.332	0.000	0.103	0.488
		70	GP1-6	3.767	0.233	1.306	0.467	0.228	2.000	0.000	0.156	0.000	0.152	0.308
		71	GP1-7	3.775	0.225	1.092	0.527	0.334	1.952	0.105	0.492	0.000	0.000	0.597
		72	GP1-8	3.759	0.241	1.500	0.278	0.222	2.000	0.000	0.313	0.000	0.074	0.388
		73	GP1-9	3.946	0.054	1.331	0.363	0.305	2.000	0.000	0.208	0.000	0.076	0.283
		74	GP1-10	3.756	0.244	1.452	0.329	0.219	2.000	0.035	0.208	0.000	0.093	0.335
		75	GP1-12	3.855	0.145	1.244	0.434	0.322	2.000	0.069	0.278	0.000	0.025	0.373
		76	GP1-13	3.623	0.377	1.058	0.613	0.329	2.000	0.123	0.455	0.000	0.003	0.581
		77	GP1-14	3.980	0.020	1.272	0.431	0.298	2.000	0.069	0.086	0.000	0.047	0.202
		78	GP1-15	3.582	0.418	1.004	0.650	0.346	2.000	0.140	0.334	0.000	0.075	0.549
		79	GP1-16	3.990	0.010	1.216	0.403	0.368	1.986	0.088	0.245	0.140	0.000	0.473
		80	GP1-17	3.849	0.151	1.218	0.416	0.366	2.000	0.052	0.243	0.000	0.085	0.380
		81	GP1-18	3.834	0.166	1.319	0.363	0.319	2.000	0.138	0.155	0.000	0.027	0.320
		82	GP1-19	3.716	0.284	1.296	0.417	0.287	2.000	0.104	0.313	0.000	0.025	0.442
		83	GP1-20	3.672	0.328	1.309	0.383	0.309	2.000	0.104	0.174	0.000	0.127	0.405
		84	GP1-21	3.843	0.157	1.349	0.329	0.323	2.000	0.069	0.121	0.000	0.110	0.301
		85	GP1-22	3.774	0.226	1.235	0.452	0.313	2.000	0.104	0.296	0.000	0.017	0.417
		86	GP1-23	3.762	0.238	1.305	0.399	0.296	2.000	0.069	0.191	0.000	0.102	0.362
		87	GP1-24	3.687	0.313	1.102	0.629	0.175	1.906	0.210	0.349	0.000	0.000	0.559
		88	GP1-25	3.640	0.360	1.251	0.420	0.280	1.951	0.228	0.333	0.000	0.000	0.560
Homoionized	Ca	89	GP3-11	3.722	0.278	0.864	0.544	0.597	2.005	0.316	0.228	0.000	0.000	0.544
		90	GP3-19	3.522	0.478	1.239	0.336	0.460	2.035	0.177	0.478	0.000	0.000	0.655
	K	91	GP-3-2	3.579	0.421	1.298	0.368	0.333	2.000	0.158	0.439	0.000	0.000	0.596
		92	GP-3-3	3.664	0.336	1.080	0.389	0.531	2.000	0.159	0.549	0.000	0.000	0.708
		93	GP-3-4	3.890	0.110	1.157	0.451	0.417	2.025	0.087	0.278	0.000	0.000	0.365
		94	GP-3-6	3.863	0.137	1.145	0.537	0.346	2.028	0.104	0.191	0.000	0.000	0.294
		95	GP-3-7	3.397	0.603	1.584	0.196	0.213	1.994	0.053	0.729	0.000	0.000	0.783
		96	GP-3-10	3.632	0.368	1.325	0.419	0.297	2.041	0.140	0.262	0.000	0.000	0.402
		97	GP-3-11	3.843	0.157	1.113	0.522	0.348	1.983	0.174	0.209	0.000	0.000	0.383
		98	GP-3-15	3.806	0.194	1.196	0.539	0.243	1.978	0.087	0.330	0.000	0.000	0.417
		99	GP-3-16	3.745	0.255	1.548	0.210	0.315	2.073	0.000	0.350	0.000	0.000	0.350
		100	GP-3-20	3.783	0.217	1.265	0.366	0.349	1.979	0.157	0.314	0.000	0.000	0.471
		101	GP-3-21	3.849	0.151	1.184	0.624	0.225	2.033	0.035	0.208	0.000	0.000	0.243
		102	GP-3-22	3.711	0.289	1.469	0.211	0.299	1.979	0.106	0.440	0.000	0.000	0.545
		103	GP-3-25	3.696	0.304	1.360	0.368	0.228	1.955	0.123	0.420	0.000	0.000	0.543

858

859

860

861 **Supplementary Figure 1:** Diffractograms of air-dried oriented aggregates of the <2 μm
862 fraction, for: a. The smectite- and palygorskite-rich fault gouge from Galera Village. and b. The
863 sepiolite-rich gouge from the Rambla de los Pilares sector. Mineral abbreviations for clay
864 minerals according to Bergaya et al. (2006), Kaol: kaolinite, K-Mica: white mica (including illite
865 and muscovite), Sep: sepiolite, Sm: smectite, Pal: palygorskite. Non-clay minerals according to
866 Whitney and Evans (2010), Chl: chlorite, Dol: dolomite, Pg: paragonite, Qz: quartz. The
867 diffractogramswere obtained in a PANalytical X'Pert Pro diffractometer (CuKα radiation, 45 kV,
868 40 mA) equipped with an X'Celerator solid-state linear detector, using a step increment of 0.008°
869 2θ and a counting time of 10 s/step (Department of Mineralogy and Petrology, University of
870 Granada).

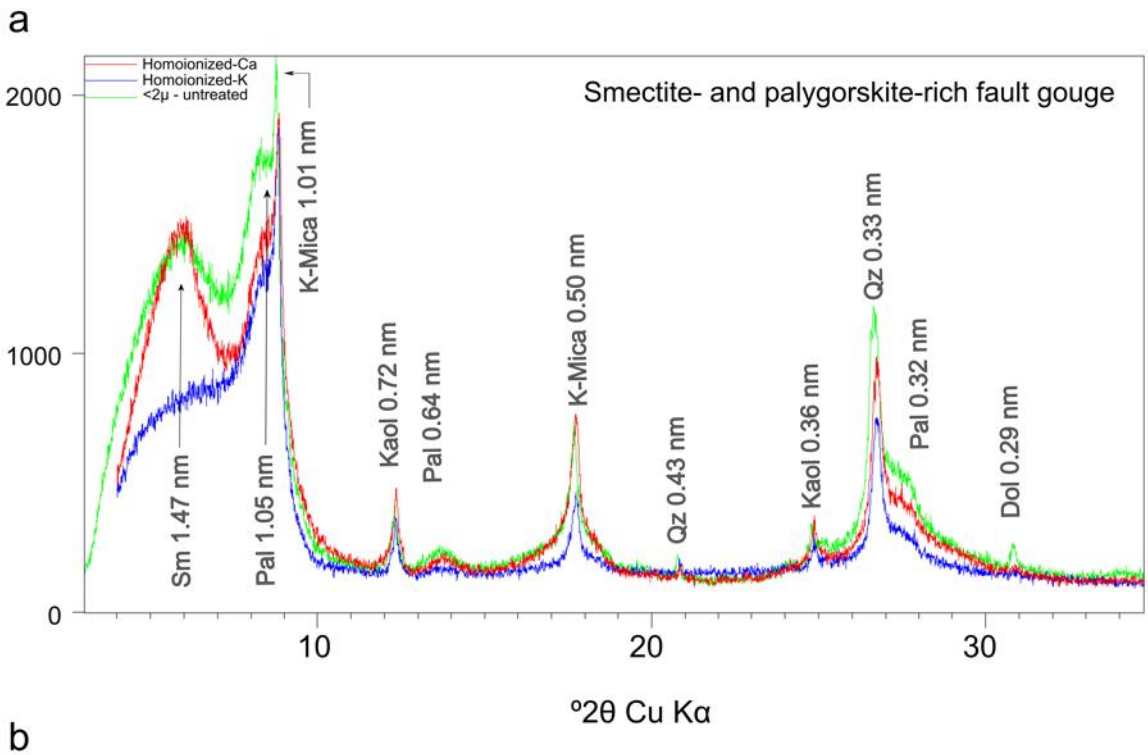
a
Homoionized-Ca
Homoionized-K
<2μ - untreated
Smectite- and palygorskite-rich fault gouge
Sm 1.47 nm
Pal 1.05 nm
K-Mica 1.01 nm
Kaol 0.72 nm
Pal 0.64 nm
K-Mica 0.50 nm
Qz 0.43 nm
Kaol 0.36 nm
Qz 0.33 nm
Pal 0.32 nm
Dol 0.29 nm
2000
1000
0
10
20
30
°2θ Cu Kα

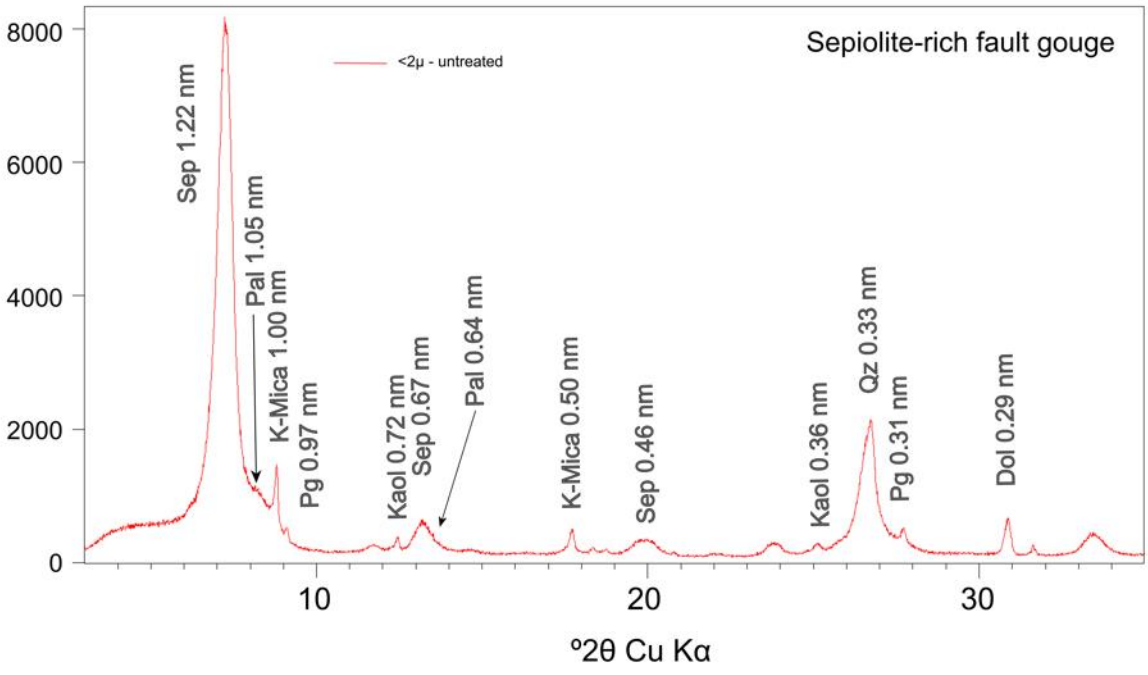
b
<2μ - untreated
Sepiolite-rich fault gouge
Sep 1.22 nm
Pal 1.05 nm
K-Mica 1.00 nm
Pg 0.97 nm
Kaol 0.72 nm
Sep 0.67 nm
Pal 0.64 nm
K-Mica 0.50 nm
Sep 0.46 nm
Kaol 0.36 nm
Qz 0.33 nm
Pg 0.31 nm
Dol 0.29 nm
8000
6000
4000
2000
0
10
20
30
°2θ Cu Kα

871

872

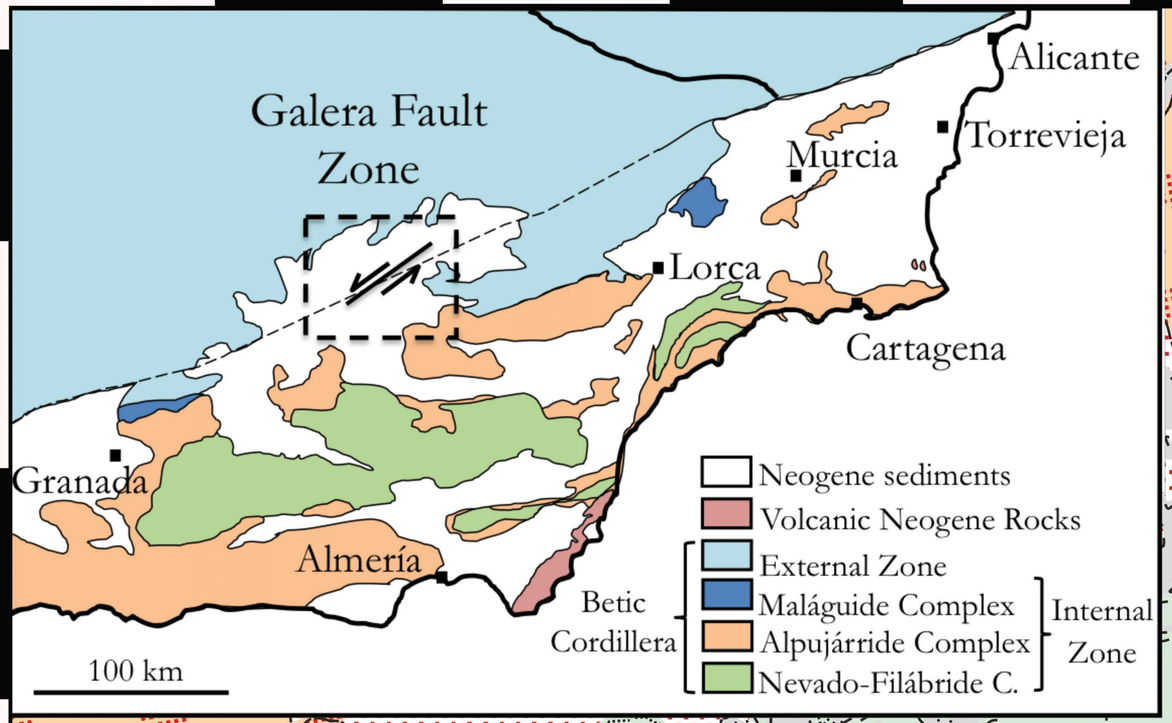

37°52'N

37°38'N

2°46'W

2°24'W

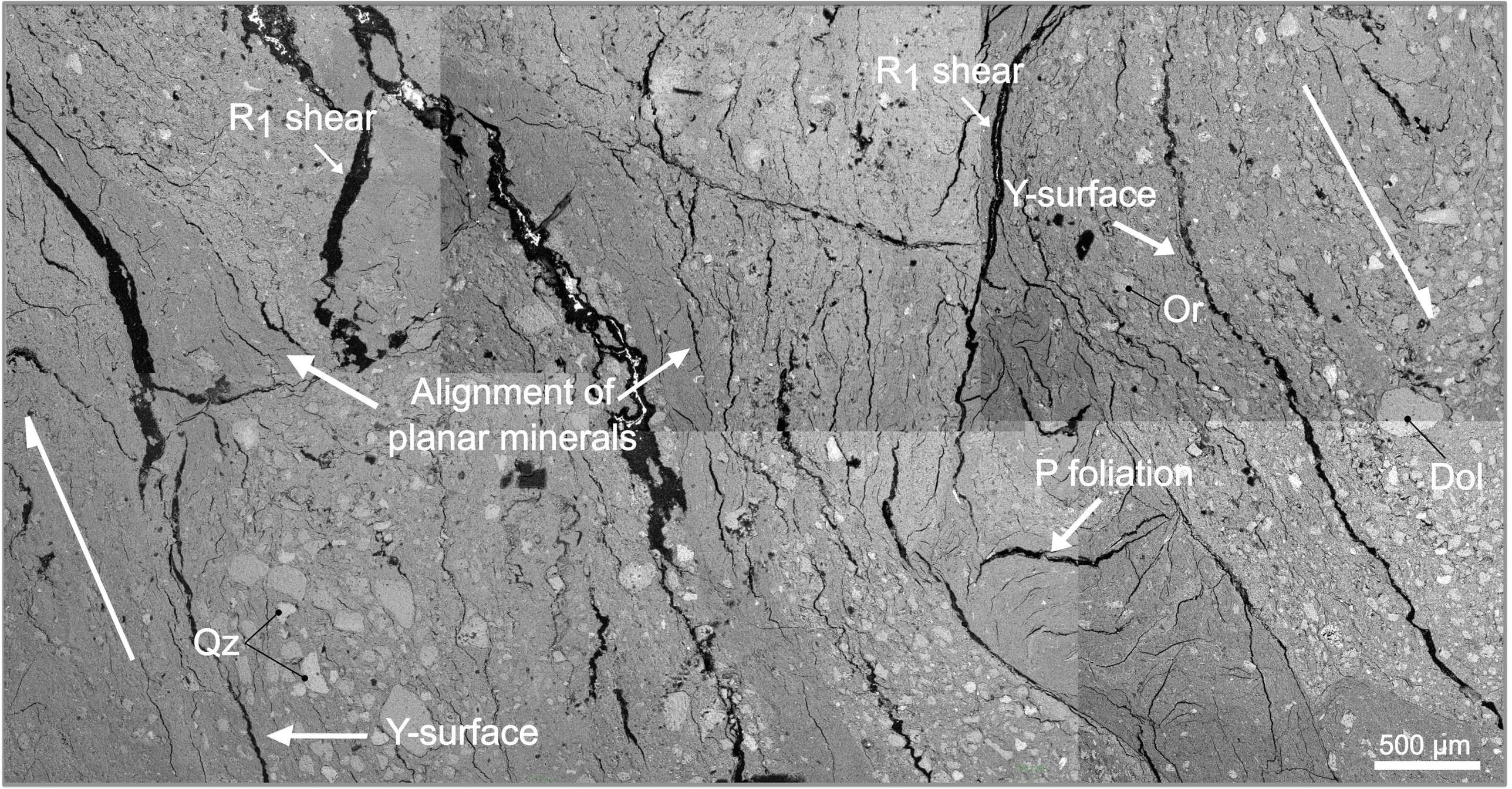
R1 shear
R1 shear
Y-surface
Or
Alignment of
planar minerals
P foliation
Dol
Qz
Y-surface
500 µm

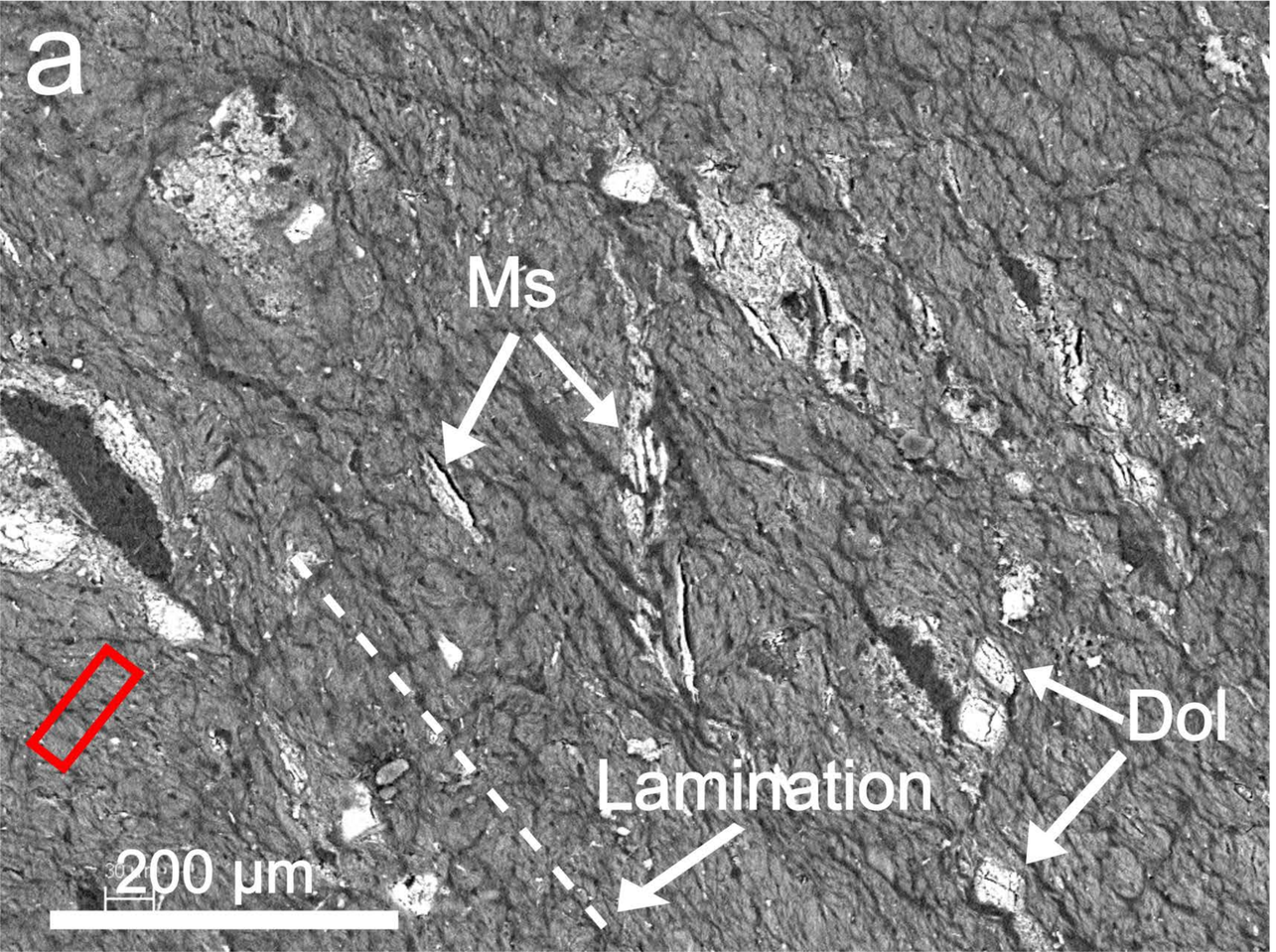
a
Ms
Dol
Lamination
200 µm

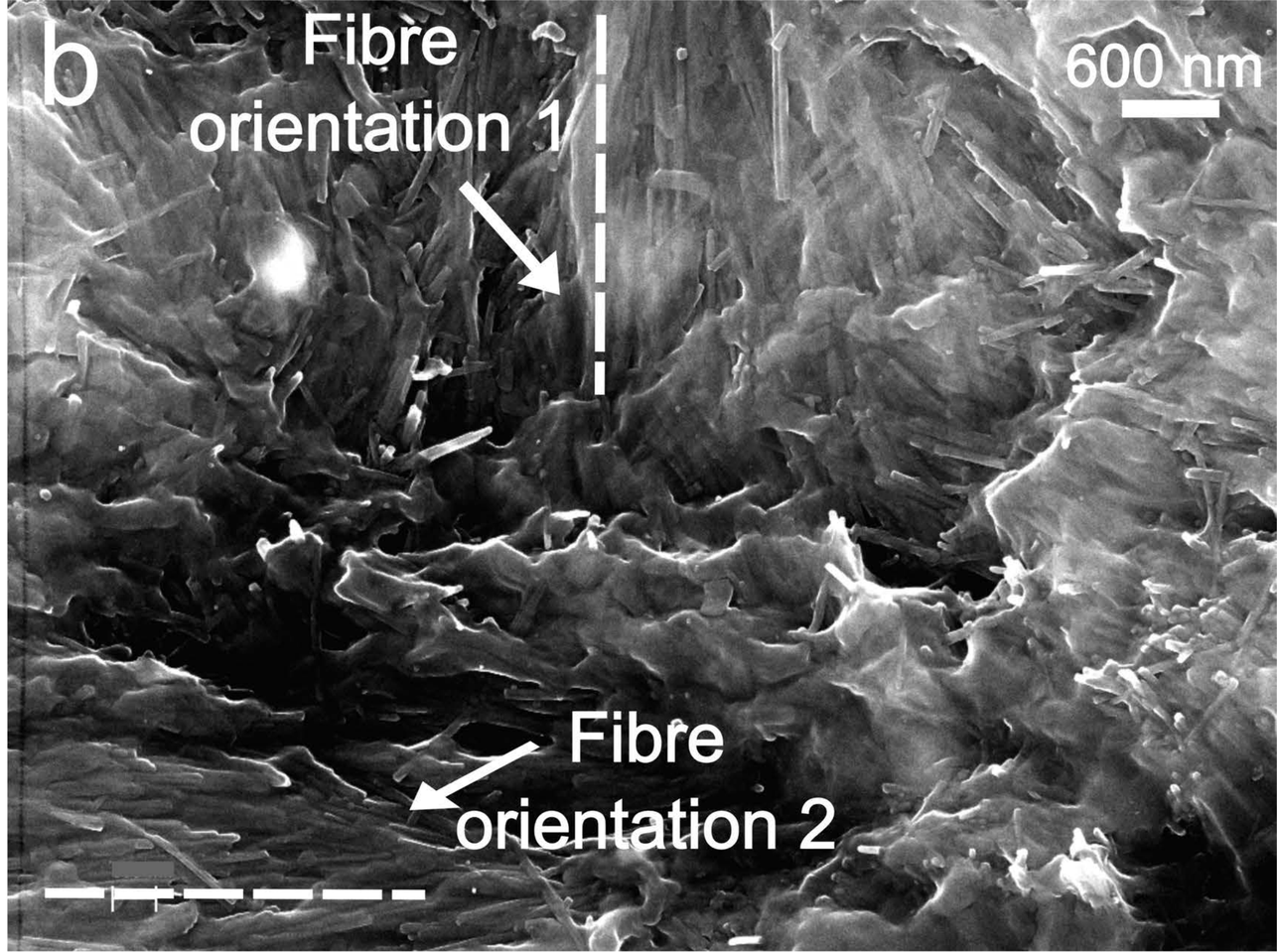
b
Fibre
orientation 1
600 nm
Fibre
orientation 2

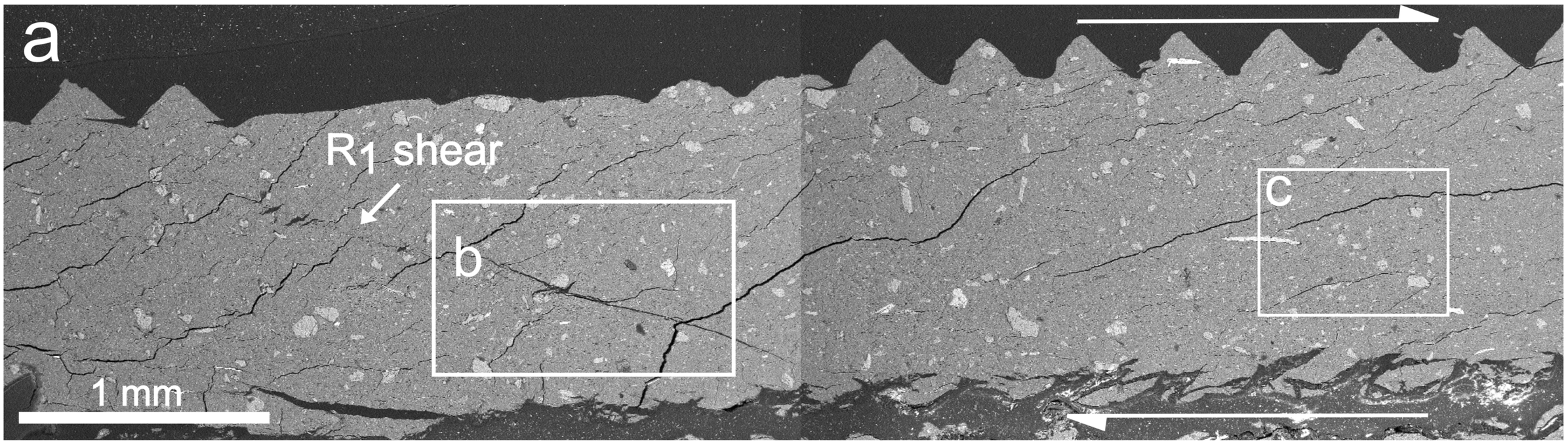
a
R1 shear
b
c
1 mm

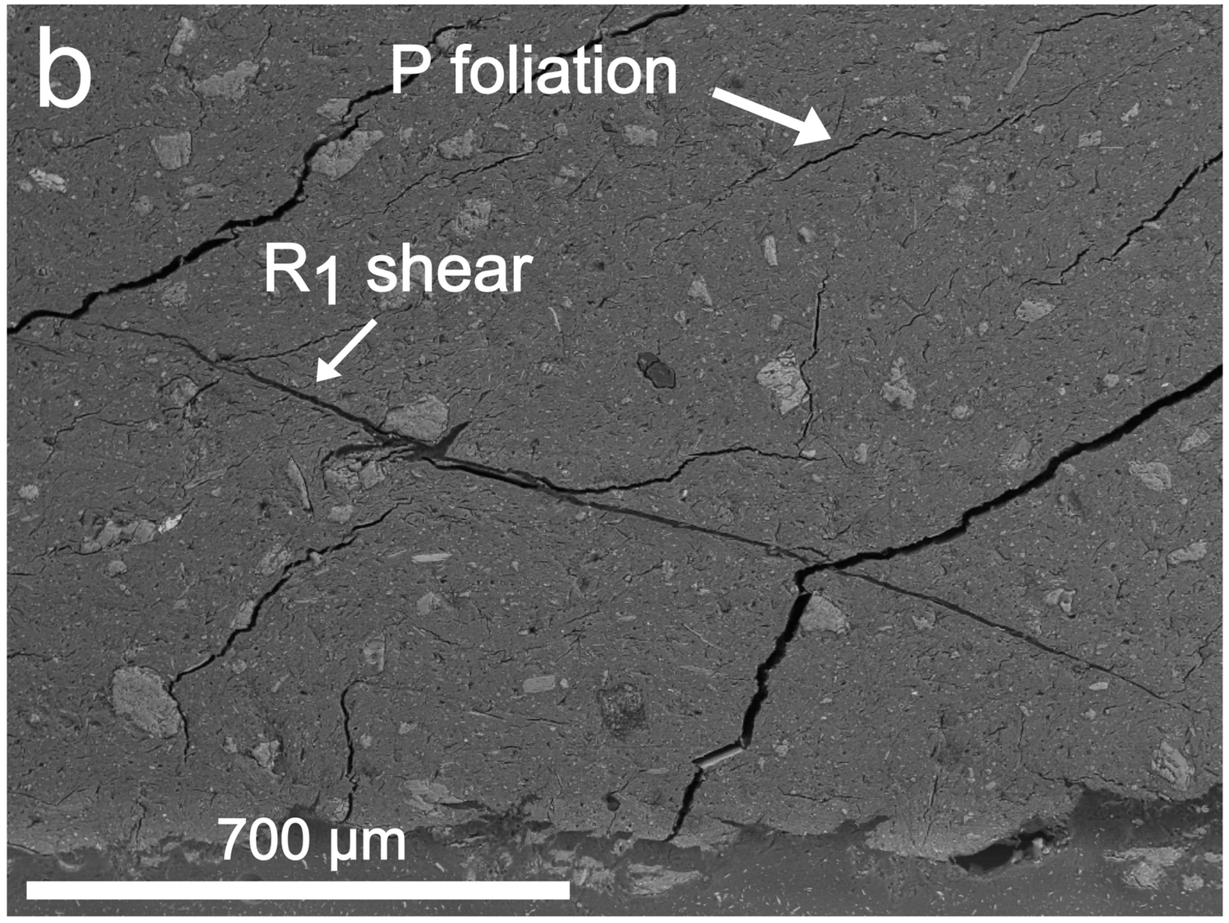
b
P foliation
R1 shear
700 µm

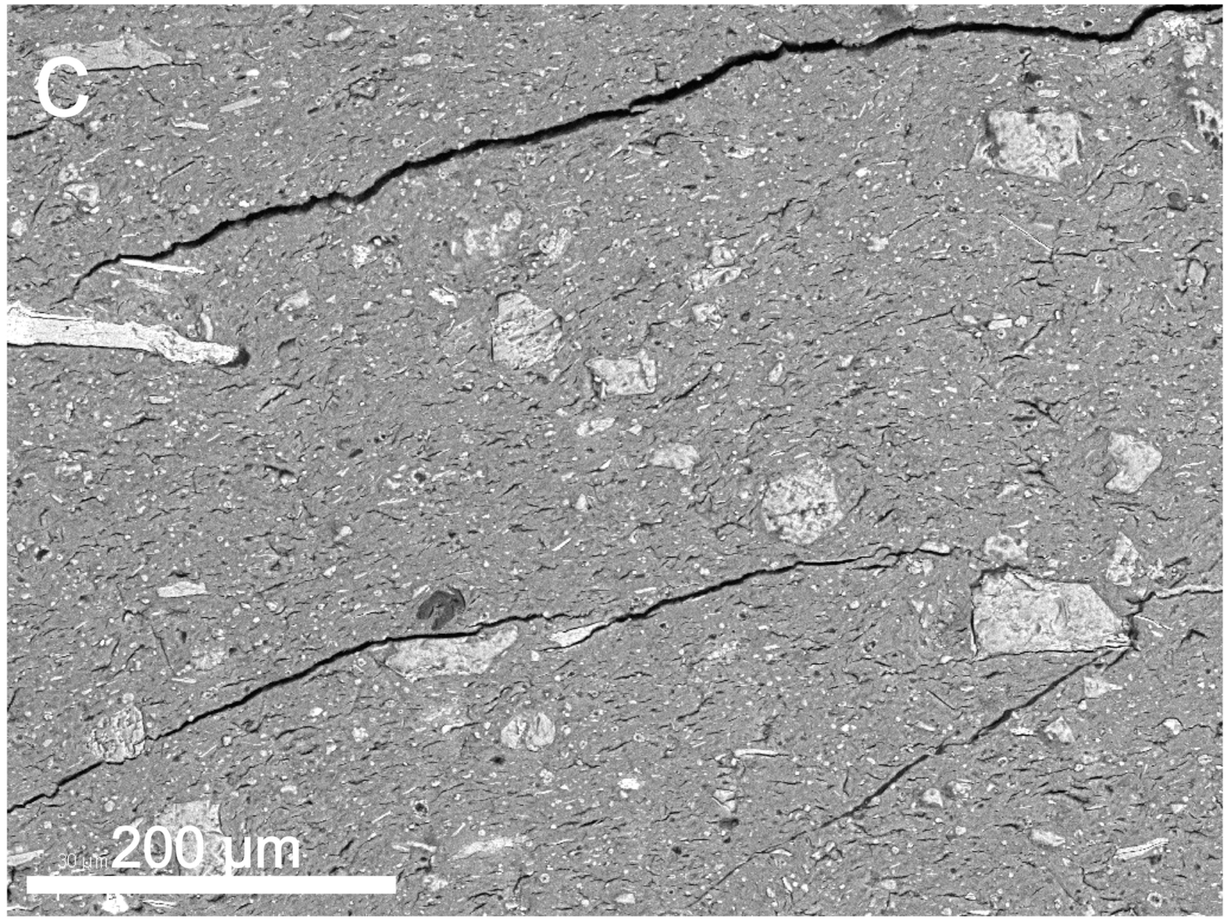
c
200 µm

a

b

200 µm

b

c

100 µm

c

R_1 shear

30 µm

d

P foliation

Mica delamination

30 µm

e

P foliation

20 µm

f

Trail

R_1 shear

20 µm

a

R_1 shear

b

c

d

100 µm

400 µm

b

R_1 shear

20 µm

100 µm

c

Boundary shear

20 µm

100 µm

d

10 µm

100 µm

e

Sense of shear

300 µm

f

Sense of shear

300 µm

a

b

c

Incipient R_1 shear

300 µm

b

Incipient R_1 shear

100 µm

c

Incipient R_1 shear

100 µm

d

Incipient R_1 shear

1 µm

500 nm

Sense of shear

e

Incipient R_1 shear

1 µm

Sense of shear

f

a
Sme
Elongated porosity
Ilt
100 nm

b
Sme
Or
Ilt
Dol
0.2 µm

c
1.05 nm
Sme
20 nm

d
2.30 nm
2.00 nm
1.30 nm
Sme
20 nm

e
Sme
Ilt
1.00 nm
20 nm

f
2.00 nm
1.94 nm
2.40 nm
20 nm

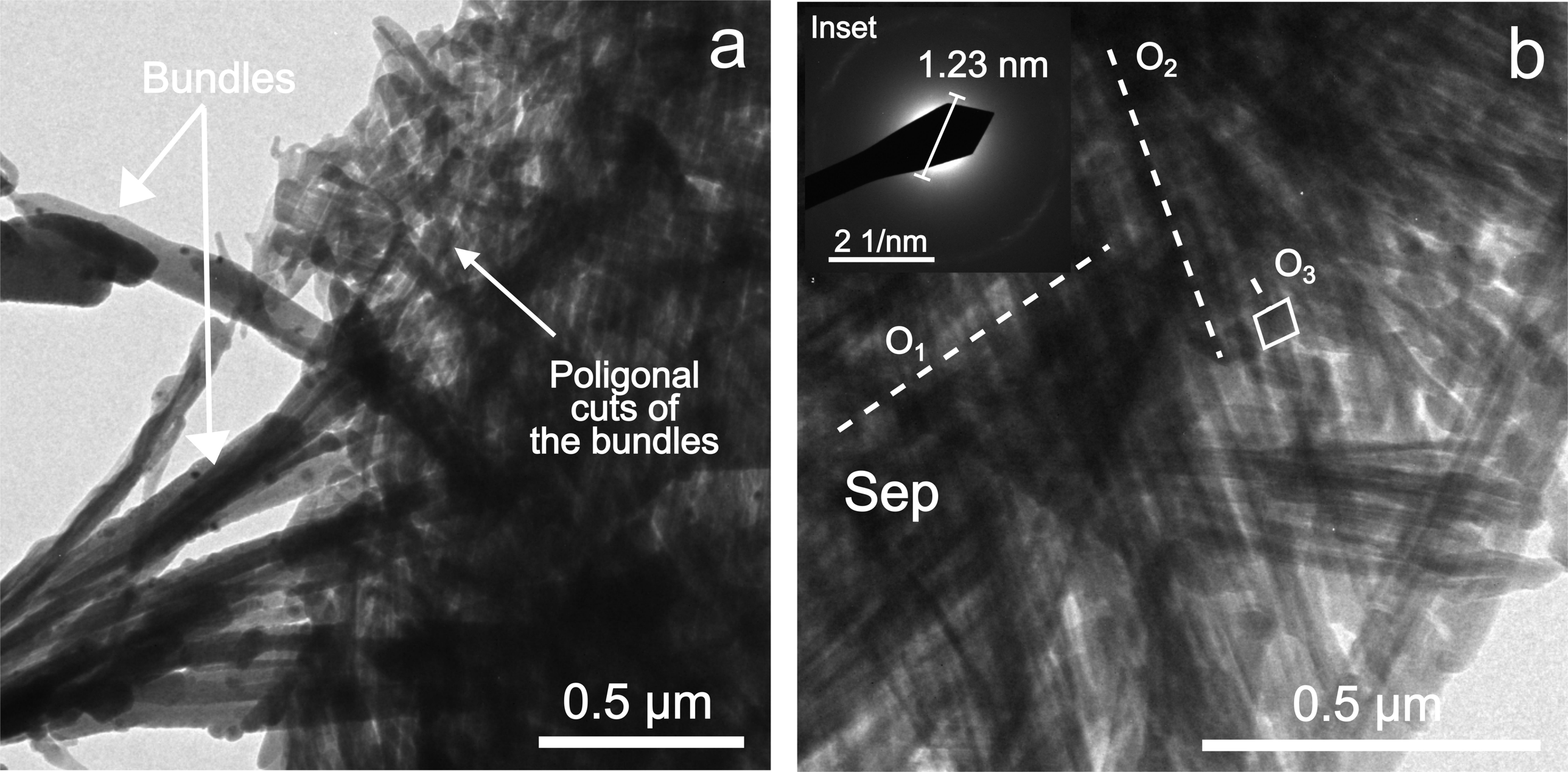
a
Bundles
Poligonal
cuts of
the bundles
0.5 μm
b
Inset
1.23 nm
2 1/nm
O2
O3
O1
Sep
0.5 μm

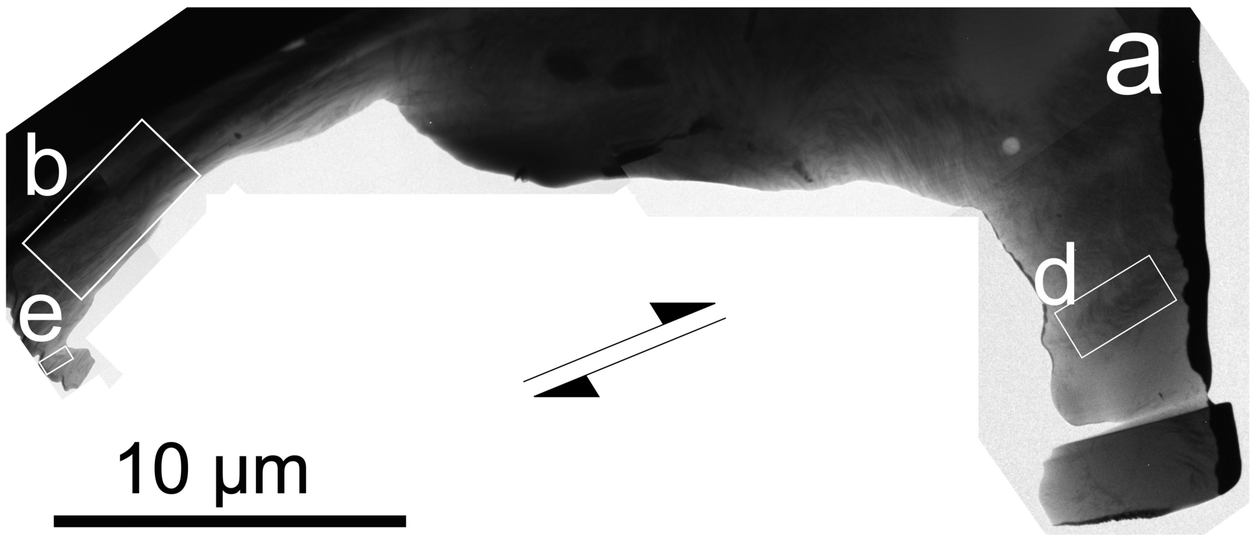
a
b
d
e
10 µm

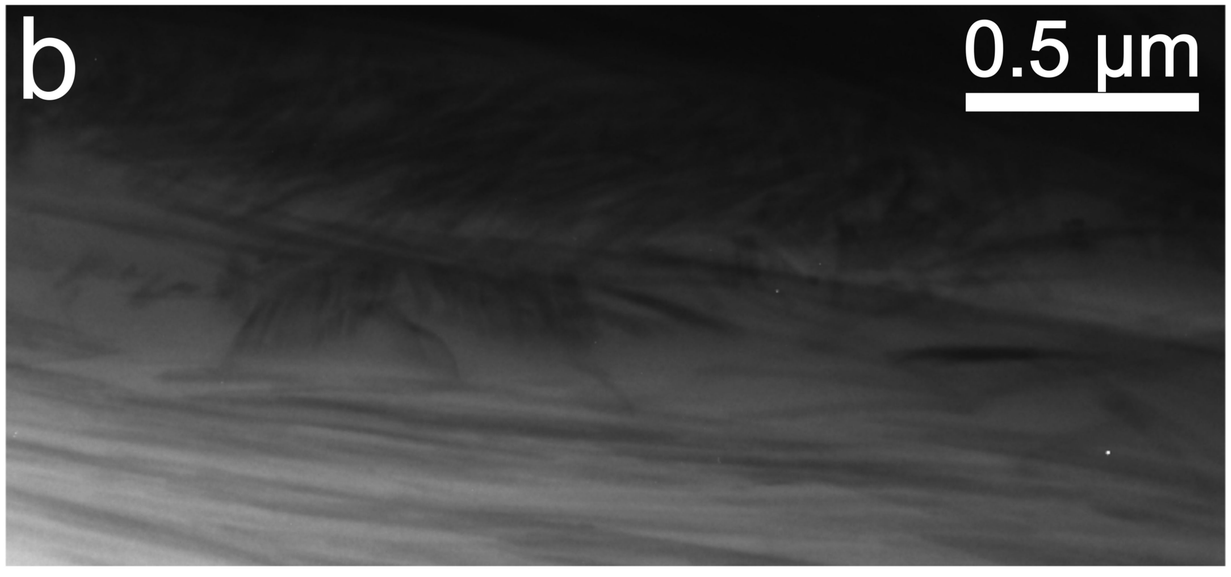
b
0.5 µm

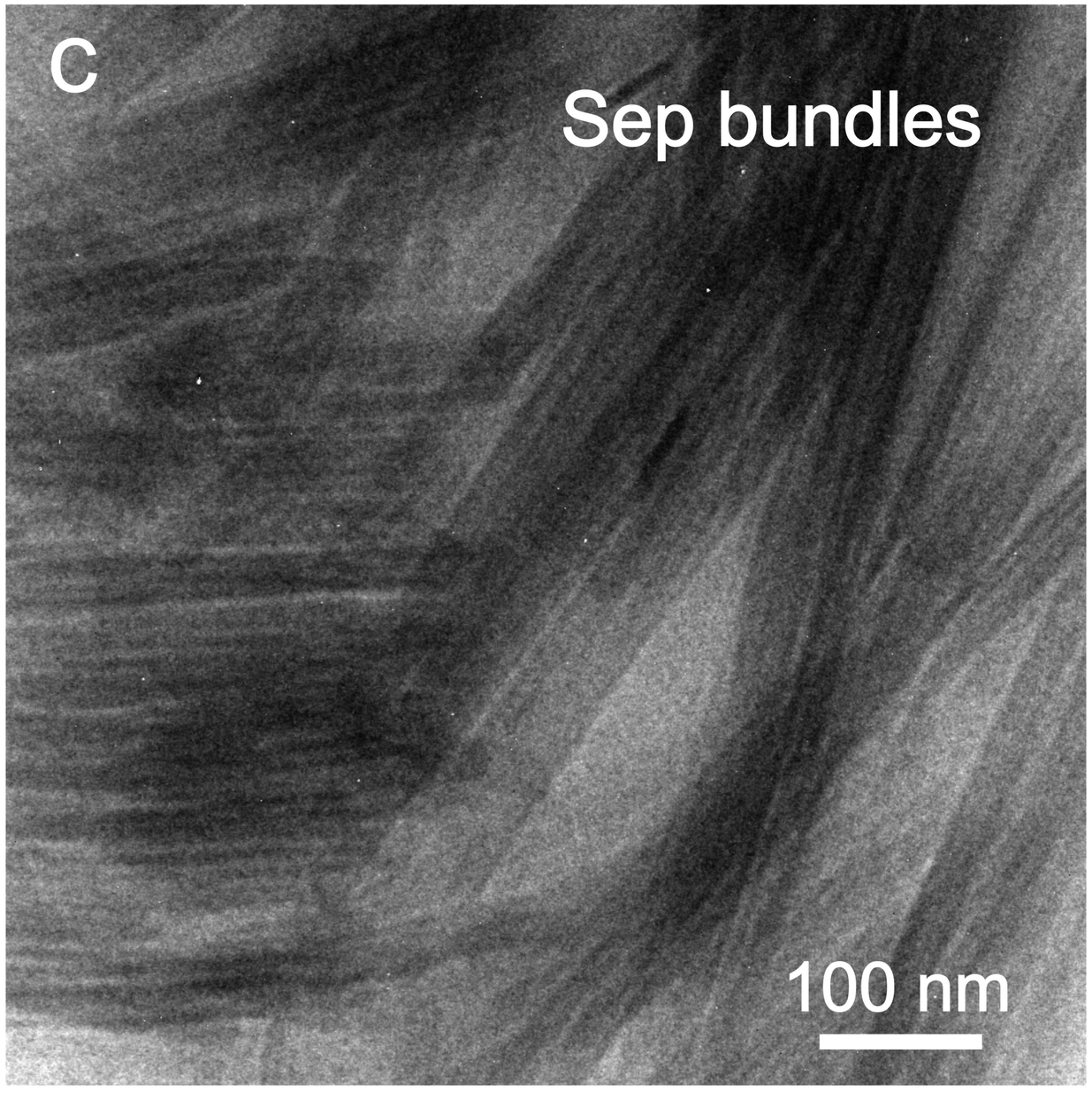
c
Sep bundles
100 nm

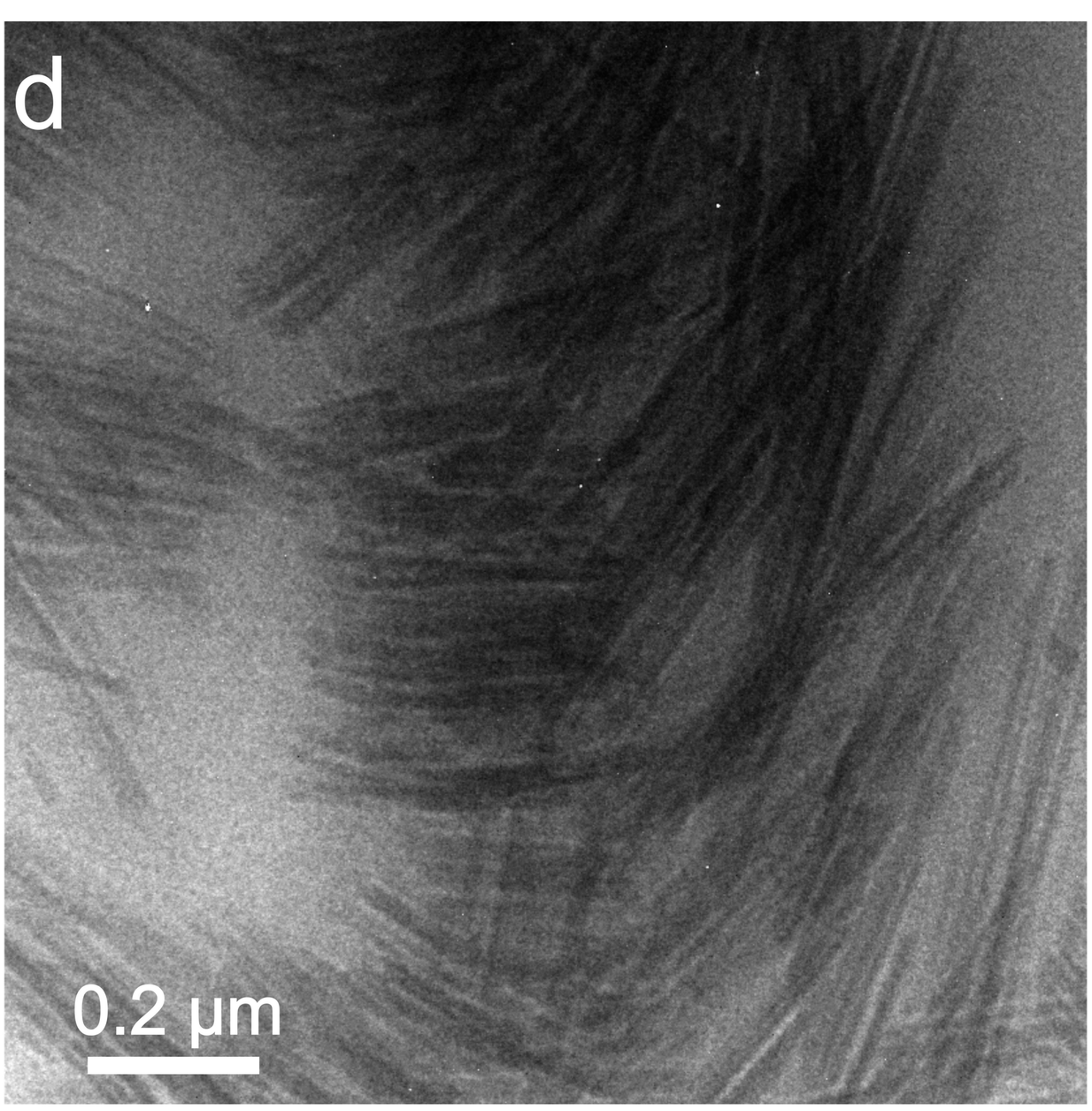
d
0.2 µm

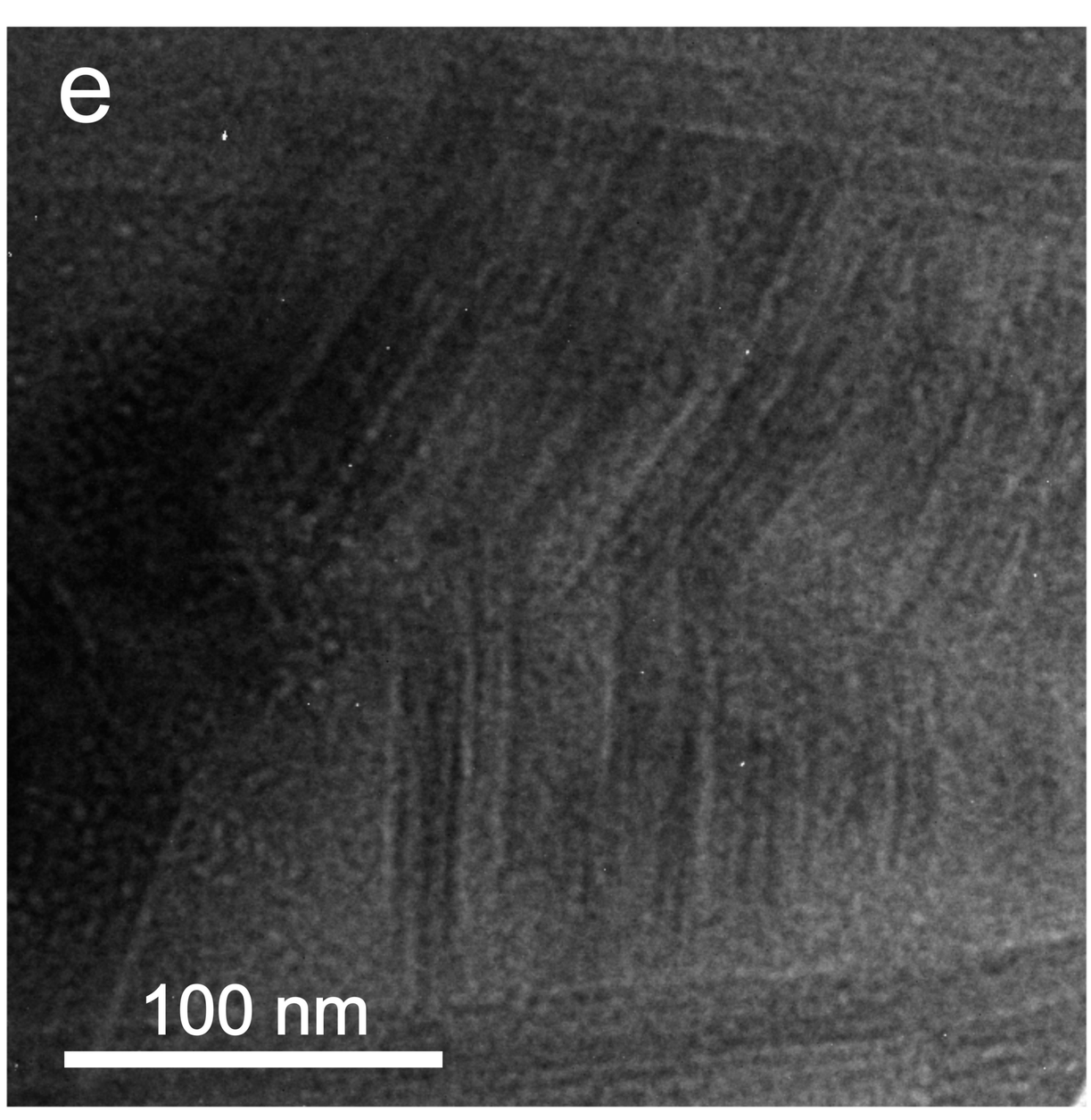
e
100 nm

a

1.20 nm

B

A

1.21 nm

Sep

10 nm

Intensity profile A

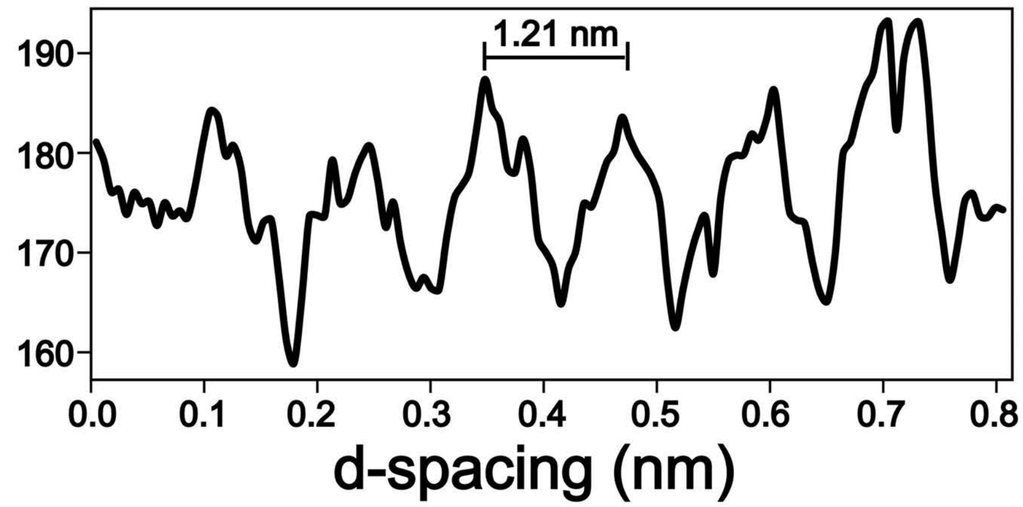

Intensity profile B

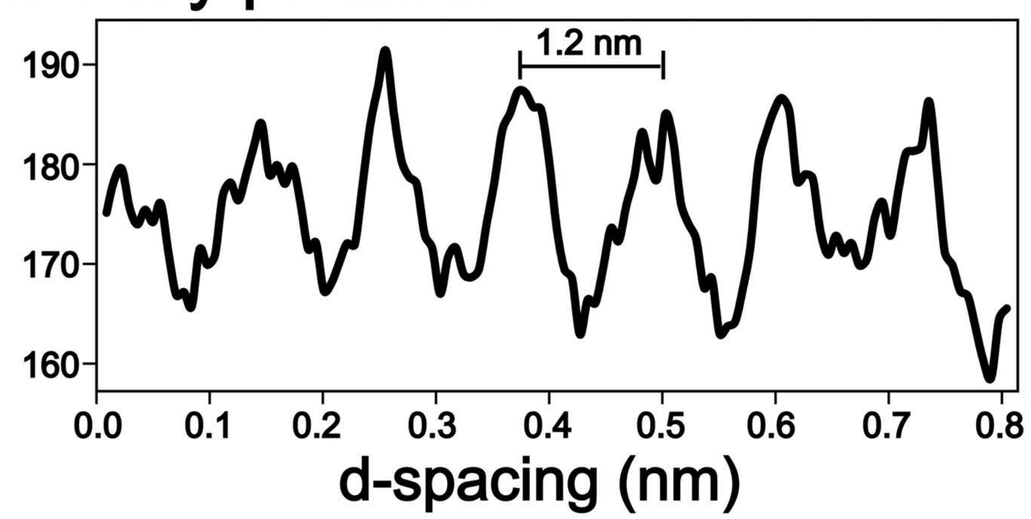

b

Sep

B

1.24 nm

1.19 nm

1.17 nm

A

20 nm

c

1.15 nm

1.18 nm

1.10 nm

20 nm

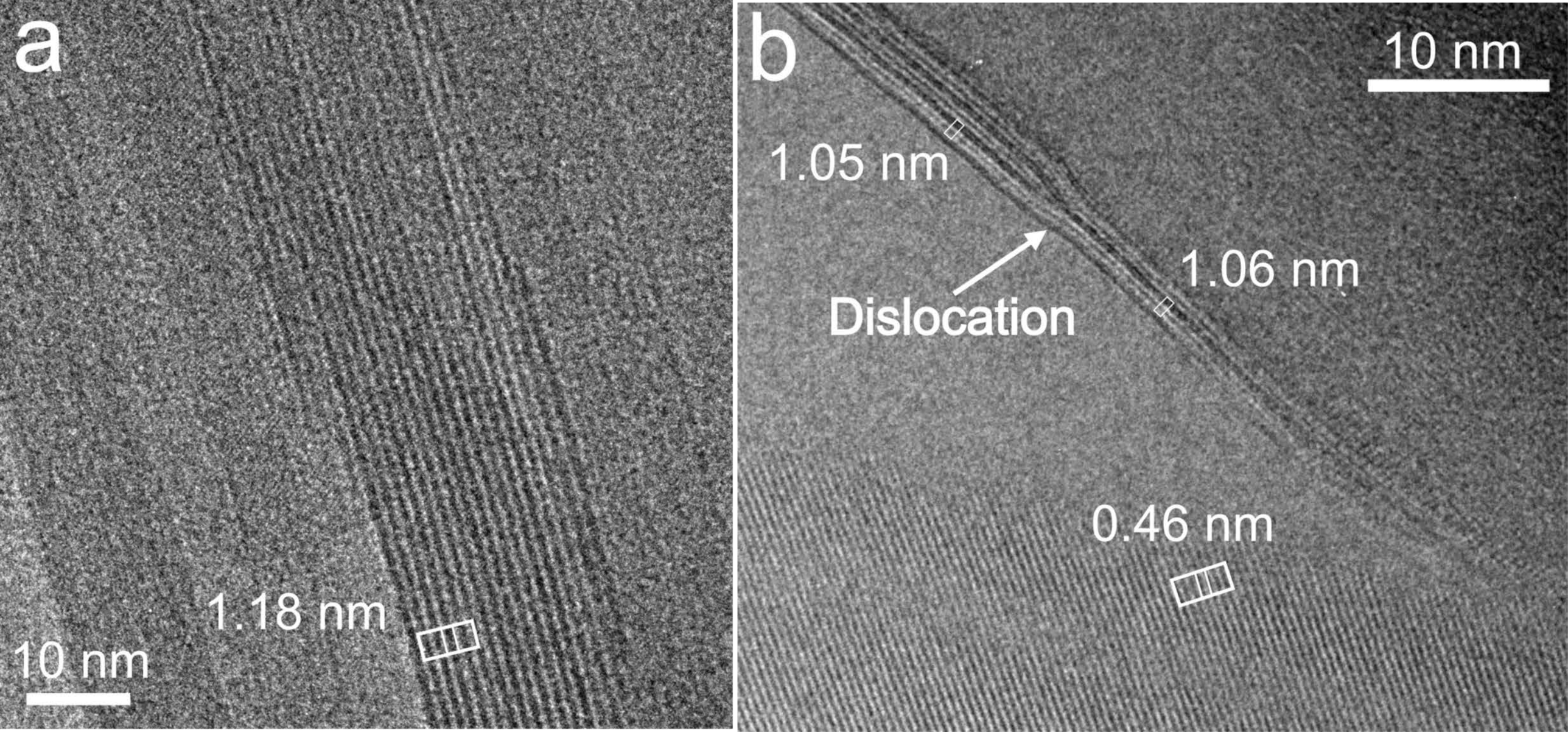
a
1.18 nm
10 nm
b
10 nm
1.05 nm
1.06 nm
Dislocation
0.46 nm

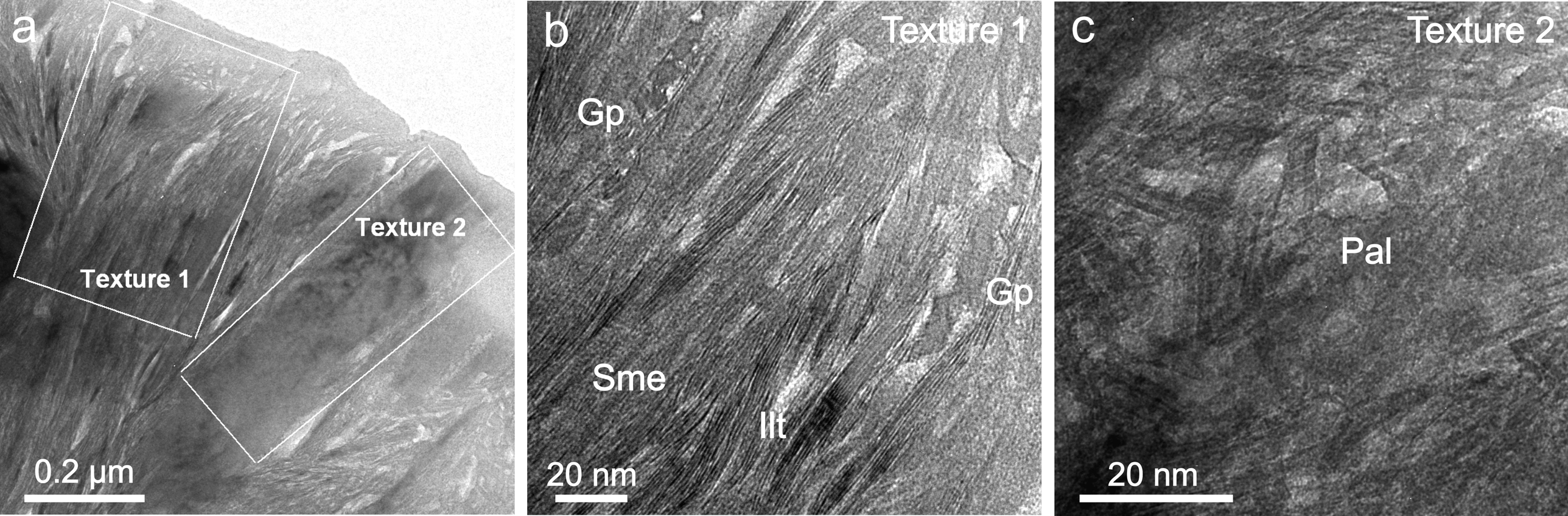
a
Texture 1
Texture 2
0.2 µm
b
Texture 1
Gp
Gp
Sme
Ilt
20 nm
c
Texture 2
Pal
20 nm

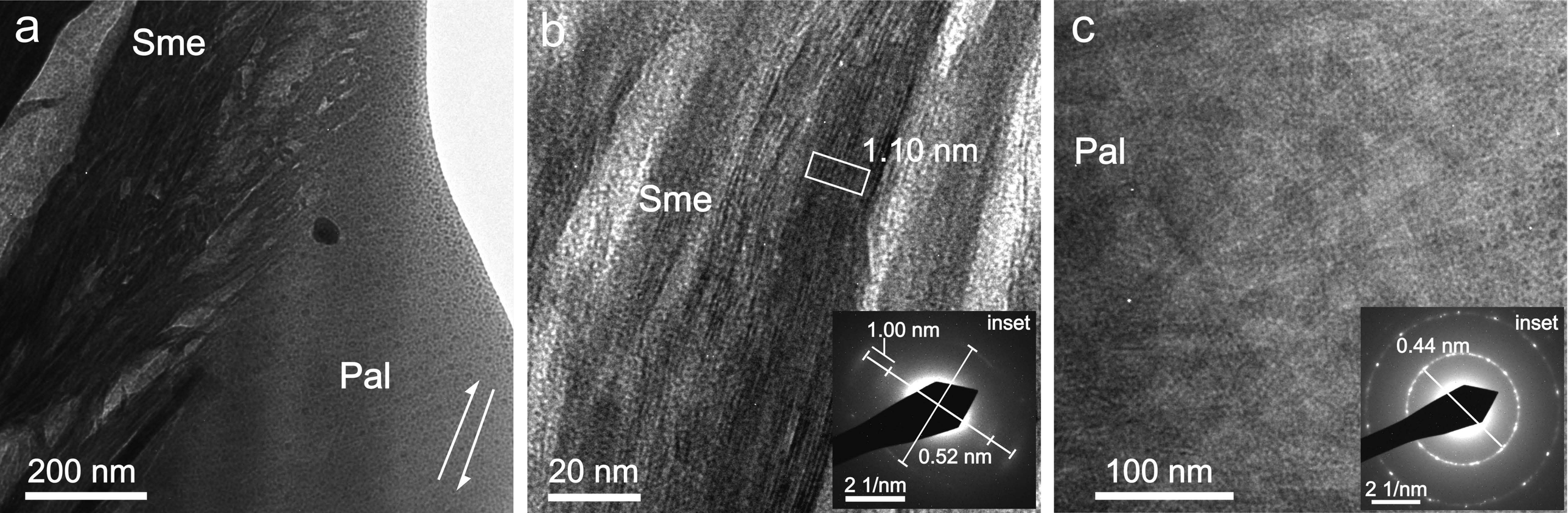
a
Sme
Pal
200 nm
b
1.10 nm
Sme
20 nm
1.00 nm
inset
0.52 nm
2 1/nm
c
Pal
100 nm
inset
0.44 nm
2 1/nm

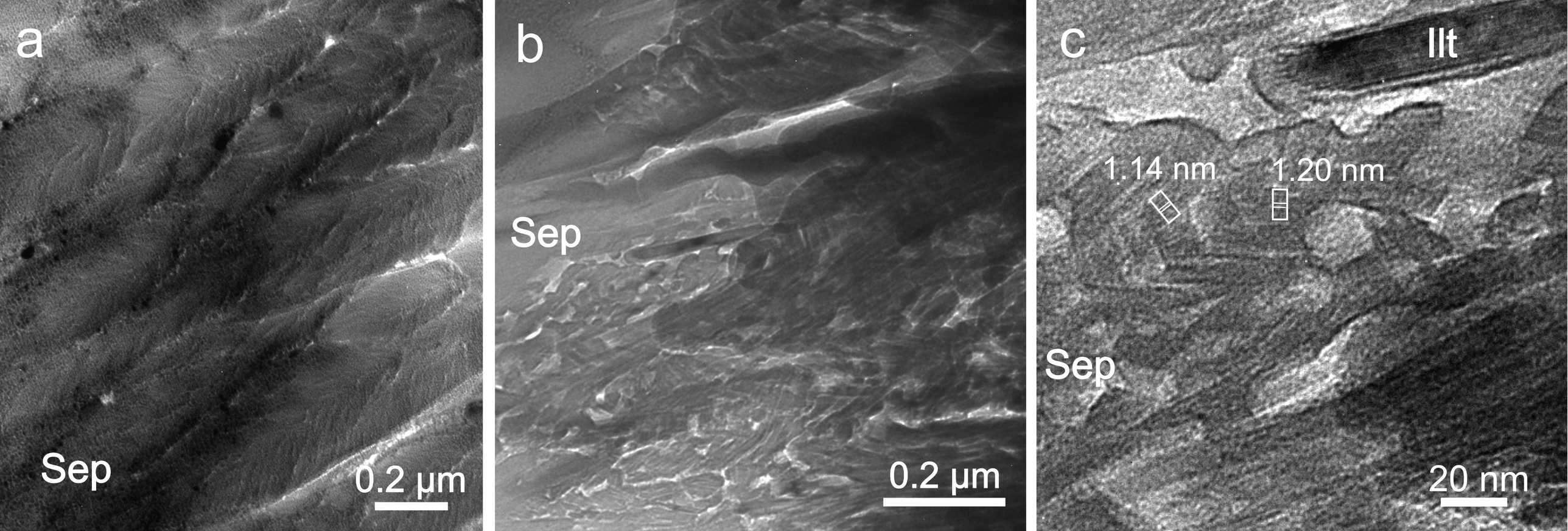
a
Sep
0.2 μm
b
Sep
0.2 μm
c
Ilt
1.14 nm
1.20 nm
Sep
20 nm

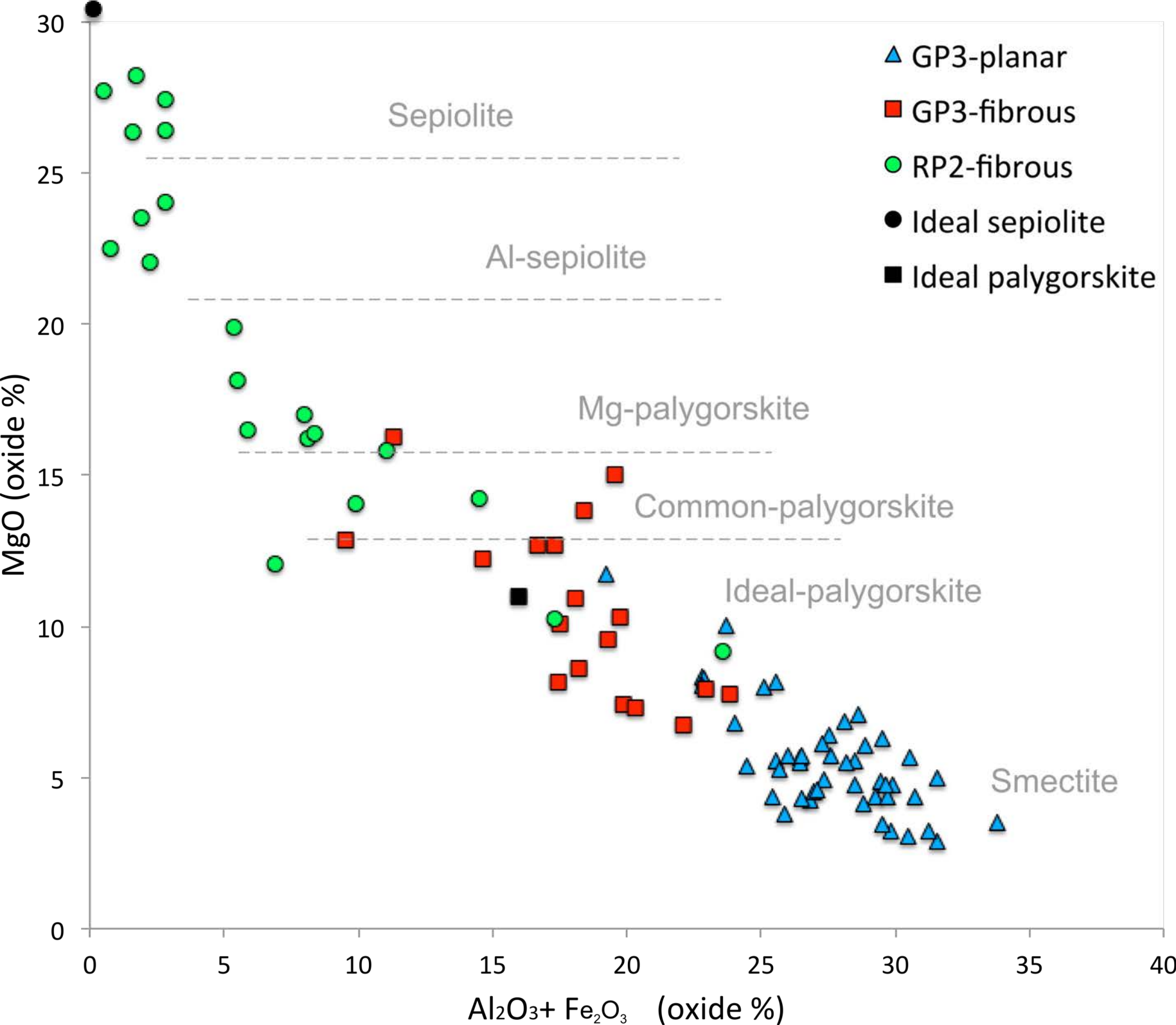
GP3-planar
GP3-fibrous
RP2-fibrous
Ideal sepiolite
Ideal palygorskite
Sepiolite
Al-sepiolite
Mg-palygorskite
Common-palygorskite
Ideal-palygorskite
Smectite
MgO (oxide %)
Al2O3+ Fe2O3 (oxide %)
0
5
10
15
20
25
30
35
40

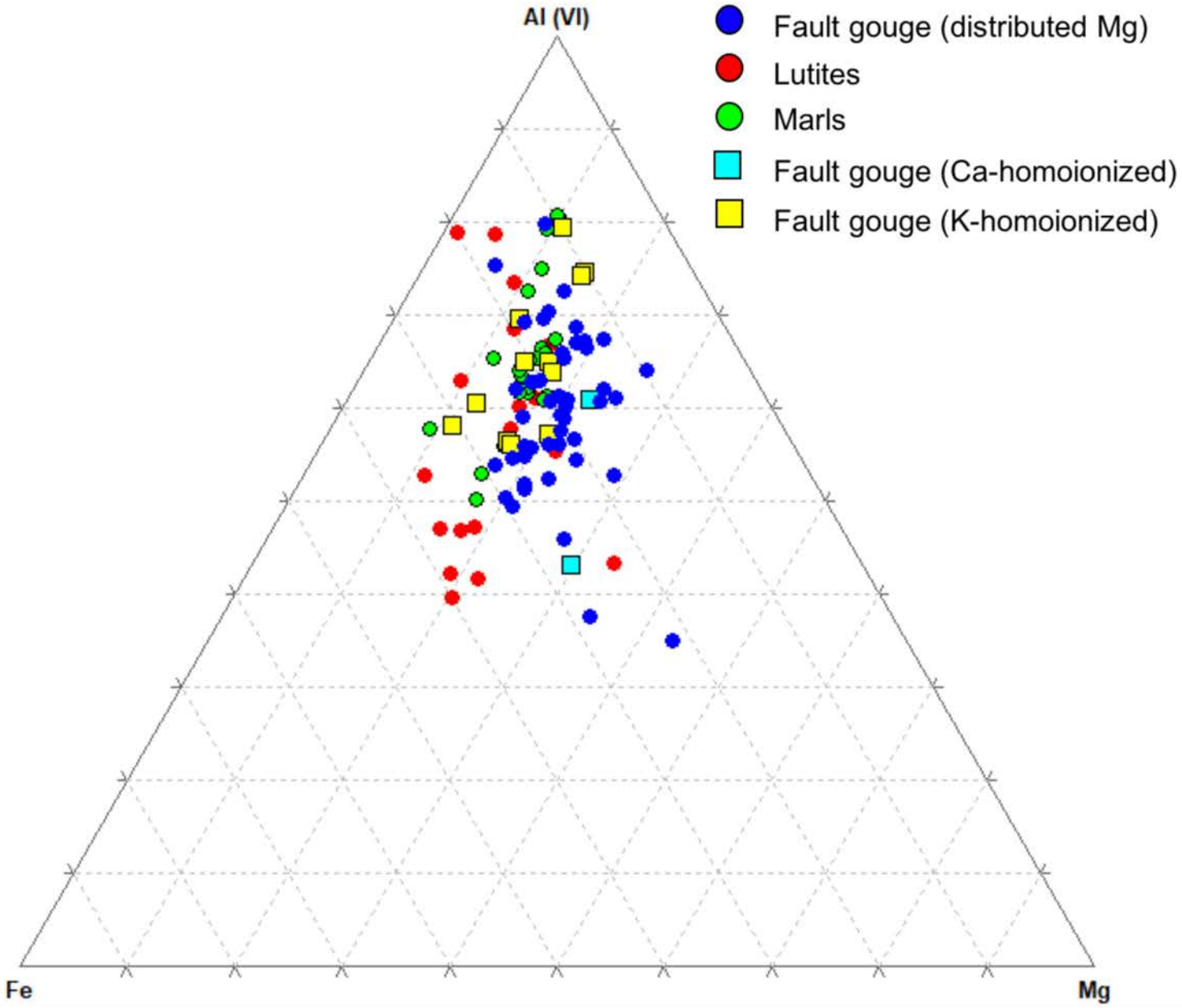
Al (VI)
Fe
Mg
Fault gouge (distributed Mg)
Lutites
Marls
Fault gouge (Ca-homoionized)
Fault gouge (K-homoionized)

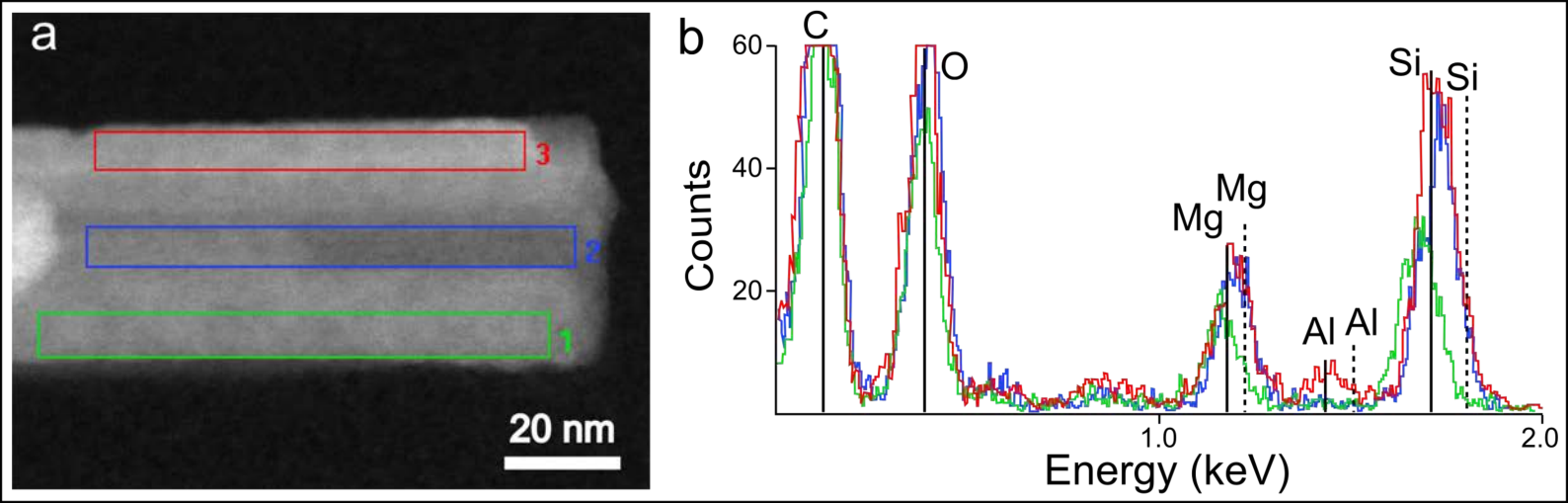
a
3
2
1
20 nm
b
C
O
Mg
Mg
Al
Al
Si
Si
60
40
20
Counts
1.0
2.0
Energy (keV)

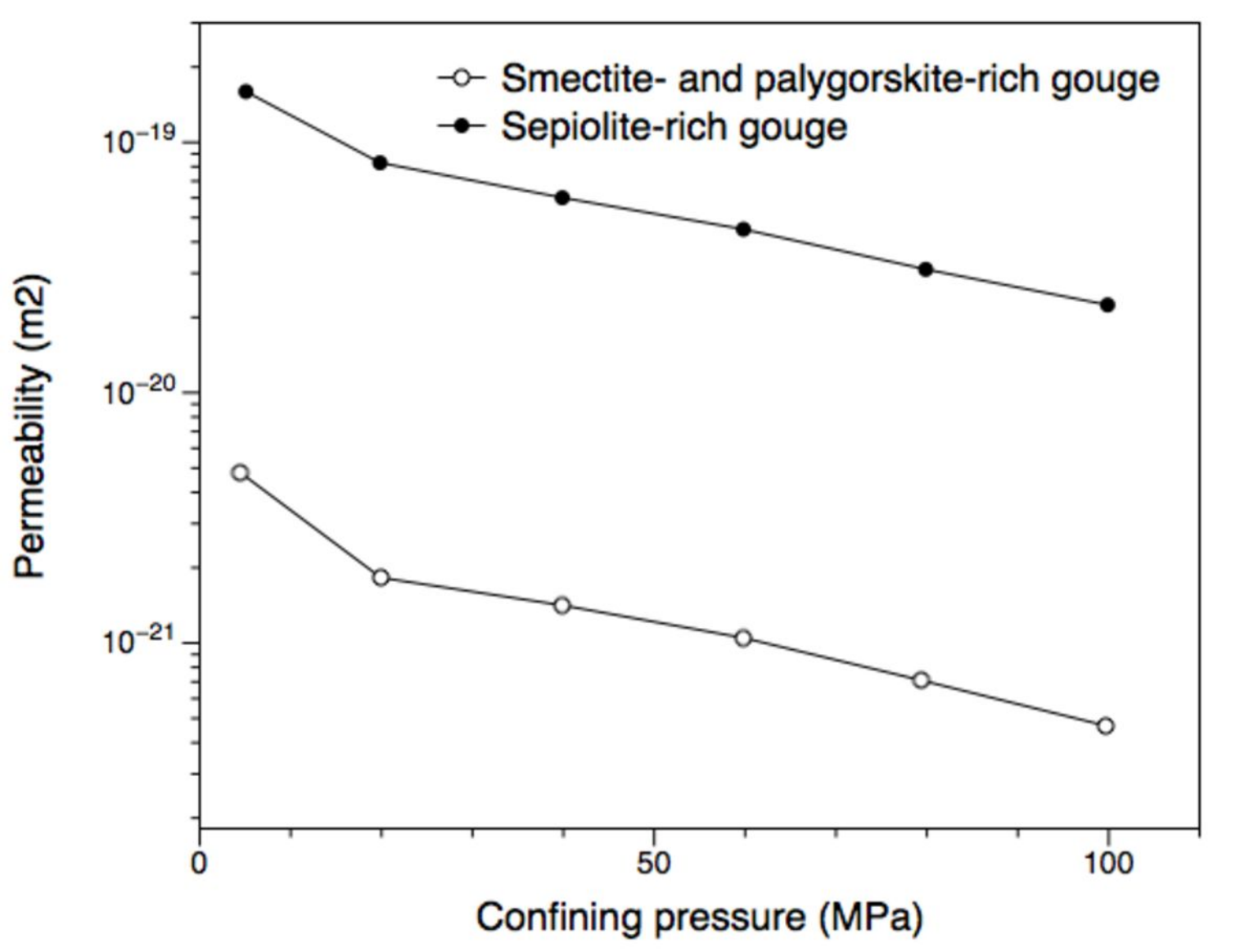
Smectite- and palygorskite-rich gouge
Sepiolite-rich gouge
Permeability (m2)
10−19
10−20
10−21
0
50
100
Confining pressure (MPa)